The Dynamics of Partial Cavity Formation, Shedding, and the Influence of Dissolved and Injected Non-Condensable Gas

Journal:	*Journal of Fluid Mechanics*
Manuscript ID	JFM-16-S-1434.R3
mss type:	Standard
Date Submitted by the Author:	n/a
Complete List of Authors:	Mäkiharju, Simo; UC Berkeley, Mechanical Engineering Ganesh, Harish; University of Michigan, Mechanical Engineering Ceccio, Steven; University of Michigan, Mechanical Engineering
Keyword:	Cavitation < Drops and Bubbles, Gas/liquid flows < Multiphase and Particle-laden Flows

Under consideration for publication in Journal of Fluid Mechanics

The Dynamics of Partial Cavity Formation, Shedding, and the Influence of Dissolved and Injected Non-Condensable Gas

Simo A. Mäkiharju[1]*, Harish Ganesh[2] and Steven L. Ceccio[2,3]

[1]Mechanical Engineering, University of California, Berkeley, CA, USA
[2]Mechanical Engineering, University of Michigan, Ann Arbor, MI, USA
[3]Naval Architecture and Marine Engineering, University of Michigan, Ann Arbor, MI, USA

In the present study, the experimental setup of Ganesh *et al.* (2016) is used to examine the dynamics of a shedding cavity by examining the vapor production rate of the natural cavity and determining how minimal injection of non-condensable gas can substantially alter the vapor production rate, the resulting cavity flow, and the cavity shedding process. The influence of the dissolved gas content on the shedding natural cavity flow is also examined. High-speed visual imaging and cinemagraphic X-ray densitometry were used to observe the void fraction dynamics of the cavity flow. Non-condensable gas is injected across the span of the cavity flow at two locations: immediately downstream of the cavity detachment location at the apex of the wedge or further downstream into mid-cavity. The gas injected near the apex is found to increase the pressure near the suction peak, which resulted in the suppression of vapor formation. Hence, the injection of gas could result in a substantial *net reduction* in the overall cavity void fraction. Injection at the mid-cavity did less to suppress the vapor production and resulted in less significant modification of both the mean cavity pressure and net volume fraction. Changes in the cavity void fraction, in turn, altered the dynamics of the bubbly shock formation. Variation of the dissolved gas content alone (*i.e.* without injection) did not significantly change the cavity dynamics.

1. Introduction

From ship propellers to cryogenic rocket motors, hydrodynamic partial cavitation can significantly alter the performance of hydraulic systems and turbo-machines as discussed in Brennen (1995) and Franc & Michel (2006). In many cases, these cavities form from vaporization of the freestream fluid when local flow pressure drops below vapor pressure near a flow boundary. Artificial (*i.e*. ventilated) partial and super cavities, which are composed primarily of non-condensable gas injected into the flow, have also been used to reduce friction drag on naval objects. Amromin & Minize (2003), Kawanami & Arndt (2011), Wosnik & Arndt (2013), and Karn *et al.* (2016) examined the use of artificial cavities for drag reduction, along with Lay *et al.* (2010), Mäkiharju *et al.* (2013a) and Zverkhovskyi (2014). Ceccio (2010) provides a recent review. However, fewer studies investigate vapor cavities that have the addition of non-condensable gas into a natural cavity, and this is important mainly in the context of shedding of vapor clouds.

For a general cavity flow, it is useful to divide the cavity pressure into the contribution that is due to the presence of non-condensable gas and the fraction due to vapor pressure. When the non-condensable gas pressure is much higher than the vapor pressure, the cavity is *ventilated* or *artificial*. Conversely, when the contribution to the cavity pressure due to the presence of non-condensable gas is small compared to the vapor pressure, then it is *natural*. The difference between the cavity pressure and the vapor pressure is often referred to as the cavity *compliance*

*E-mail address for correspondence: makiharju@berkeley.edu

(Young *et al.* 2017) since the presence of non-condensable gas can lead to changes in the mechanism of condensation and gas entrainment at the cavity closure hence, altering the topology and dynamics of the cavity. Recently, Ganesh *et al.* (2016) reported the presence of propagating bubbly shock waves as a dominant mechanism of partial natural cavity shedding on a wedge. The properties of the shock wave depend significantly on the void fraction flow field and cavity pressure. The role of non-condensable gas in influencing in the cavity dynamics, particularly on the vapor production rate, and hence also on shock induced shedding is yet to be understood. Such an understanding would help in the active control of shedding dynamics, and hence enable improved performance by non-condensable gas injection.

Vaporous cavities with injection of small volume fluxes (relative to volume flow rate of liquid) of non-condensable gas (*e.g.* air) have been most often studied in context of dam spillway aeration (Chanson, 1994), and recently Tomov *et al.* (2016) examined the effect of introducing non-condensable gas to modify the cavitating flow in a Venturi. However, the behavior of cavities composed of mostly non-condensable gas versus those composed solely of vapor can be quite different. Young *et al.* (2017) provide a recent review of cavities forming on lifting surfaces, and the effect of ventilation. This can be contrasted with the behavior of natural cavities, as discussed in Franc & Michel (2006).

In recent decades the advances in experimental techniques, especially ones pertaining to void fraction measurement, have enabled study of the dynamics of partial cavities in greater detail, as exemplified by work of Stutz & Reboud (1997) utilizing optical probes and Stutz & Legoupil (2003) utilizing one-dimensional X-ray densitometry. While the flows of interest are highly time-dependent and three-dimensional, the recent progress to time-resolved two-dimensional void fraction measurements with a system developed by Mäkiharju *et al.* (2013b) enabled Ganesh *et al.* (2016) to experimentally identify that for natural partial cavities bubbly shock propagation can be the mechanism for sheet-to-cloud transition. In the present study, we focus further on the dynamics of the cavity forming in the apex region of the wedge used by Ganesh *et al.* (2016), specifically vapor production rates, and examine whether non-condensable gas injection can alter these mechanisms for cases where the gas injection volume flow rate is at most on the order of the vapor production rate of the natural cavity. Thus, the cavities under examination are closer to natural cavities than fully ventilated flows.

The goal of the present work is to further study the dynamics of these shedding partial cavities with bubbly shocks, their sensitivity to small perturbations in pressure and dissolved gas contents, and most importantly the effects of non-condensable gas injection when the volume rate of injection is less than or on the order of the vaporization rate of the non-injection cavity flow. The previously utilized experimental setup of Ganesh *et al.* (2016) was modified to allow for non-condensable gas injection and for additional simultaneous measurements of cavity pressures at two locations. Our observations suggest that the baseline (non-injection) cavity flow is insensitive to changes in the amount of dissolved gas over the parameter range examined. However, it was found that injection of even limited amounts of non-condensable gas at rates that are a fraction of the natural vaporization rate can significantly alter the formation and dynamics of the partial cavity by *reducing* the overall vapor production rate and therefore the average cavity void fraction. Additionally, the bubbly shock mechanism can be altered even if the total void fraction is not significantly reduced, as the speed of sound in the mixture and shock speed can be influenced *via* gas injection. Consequently, in some cases the shedding mechanism appears to shift from propagation of bubbly shocks to the one dominated by the classic re-entrant liquid jet. Both reduction of vapor production and altered cavity dynamics were related to the

increases in the mean cavity pressure at the suction peak and within the cavity itself. This increase in pressure was a consequence of gas injection.

While the previous study discussed the bubbly shock mechanism and effect of cavitation number over a wide range at cavity lengths, in the present study we will focus on vapor production rates within the cavity, and particularly the effect of gas injection on the strongly shedding condition that resulted from a bubbly shock formation and propagation. The experimental setup in described in Section 2, and in Section 3 we present our results on the dynamics of natural cavitation, including the influence of dissolved gas content. Next, results for cavitating flows with non-condensable gas injection are presented in Sections 4 and 5. A discussion and conclusions are presented in Section 6.

2. Experimental Setup

The experiments were conducted at the University of Michigan 9-inch water tunnel using a setup similar to that described in Ganesh *et al.* (2016), but with modifications that permitted gas injection. The test model consists of a nominally two-dimensional wedge placed in the 76 mm x 76 mm reduced water tunnel test section. The wedge makes an angle of 22.1 degrees to the incoming flow, and has a downstream angle of 8.1 degrees, making a contraction ratio at the wedge apex of 2/3. An additional static pressure transducer and two rows of gas injection holes were added to the wedge, and the dynamic pressure transducer locations were modified to accommodate the gas injectors. Figure 1 shows the schematics of the present experimental setup and Table 1 lists the locations of the gas injectors and transducers. The *s*-axis is oriented tangential to the wedge surface downstream of the apex and parallel to the mean flow direction, and the *n*-axis is oriented normal to the wedge surface, as shown in the figure. The length of the wedge, L_w = 178 mm, was used to normalize locations in *s* and *n*. The height of the wedge, H_w = 25.4 mm, was used to normalize the streamwise, *x*, and normal, *y*, coordinates when presenting two-dimensional void fraction distributions. The reference velocity, U_0, and static pressure, p_0, were measured 76 cm upstream of the wedge apex.

Gas was injected across two spanwise locations s/L_w = 0.004 and 0.134 downstream from the wedge apex, denoted hereafter as the "apex" injection location and the "cavity" injection location, respectively. Each gas injector consisted of a row of 72 holes spaced 1.02 mm apart at a 45 degree angle with respect to the wedge surface and with 0.51 mm diameter. The injected gas flow rate was measured for up to 2 x10^{-5} kg s^{-1} (1 slpm) with an Omega Engineering FMA-6707 and for fluxes higher than this, up to 2 x10^{-4} kg s^{-1} (10 slpm), using an Omega Engineering FMA-5520 mass flow meter with manufacturer specified accuracies of ±1% and ±1.5% of full scale, respectively. During the experiments 15 seconds were allowed from beginning of gas injection at pre-set flow rate before gathering of data to ensure the gas flow rate had reached steady state.

The static pressure was measured at two locations on the surface of the wedge *via* 0.8 mm diameter taps. The first tap, denoted as the "apex" pressure tap, was located at s/L_w = 0.013 to measure pressure p_A. The second, denoted as the "cavity" pressure tap, was located at s/L_w = 0.0147 to measure the pressure p_C. The pressure from each tap was measured by an Omega Engineering PX20-05A5V 0 to 36 kPa transducer with accuracy of ±0.08% of full scale.

The unsteady pressure on the wedge surface was measured using two flush mounted surface pressure sensors PCB 138M101 connected to a signal conditioner (ICP Sensor 480CO2) with combined accuracy of ±2% of reading. The unsteady pressure signals were sampled at a frequency of 500 kHz using a National Instruments PCI-MIO-16E-4 DAQ card triggered using

the common time base with the X-ray measurement system. The locations of the sensors are given in Table 1, and the pressures are denoted as $p_{D1}(t)$, and $p_{D2}(t)$ for the upstream and downstream transducers, respectively.

The instrumentation used to measure tunnel inlet flow velocity, inlet pressure, static and dynamic pressure on the wedge, as well as to record the high-speed video, are described in Ganesh *et al.* (2016) and the cinemagraphic X-ray system is described in Mäkiharju *et al.* (2013b). In the present study, the inlet flow velocity was fixed at U_0 = 8.0 ± 0.05 ms^{-1} and the inlet static pressure for the nominal conditions was fixed at p_0 = 70 ± 0.5 kPa. Hence, the cavitation number

$$\sigma_O = \frac{p_O - p_V}{\frac{1}{2}\rho U_O^2} \tag{3.1}$$

was fixed at σ_0 = 2.03 ± 0.01, when the water temperature is taken to be nominally constant at 20 ± 1 ^{o}C, and consequently the vapor pressure to be a constant p_V =2.3 ± 0.2 kPa and the water density ρ = 998 ± 0.5 kg m^{-3}. We also will define two cavitation numbers based on apex and cavity mean static pressures, p_A and p_C

$$\sigma_A = \frac{p_A - p_V}{\frac{1}{2}\rho U_O^2} \tag{3.2}$$

And

$$\sigma_C = \frac{p_C - p_V}{\frac{1}{2}\rho U_O^2} \tag{3.3}$$

The dissolved oxygen content was varied using a closed loop deaeration system, and the free-stream value was measured using an Orion Start A113 dissolved oxygen meter to a precision of ±2%. The dissolved oxygen values during the experiment varied from 30% to 75% of saturation at STP, and here the dissolved oxygen is assumed to be a suitable proxy for the total dissolved gas content, as discussed by Lee *et al.* (2016).

3. Natural Shedding Partial Cavity and the Influence of Dissolved Gas Contents

We will begin with further examination of the natural cavitation occurring for the strongly shedding condition. We do this *i*) to better characterize the uncertainty in the baseline flow before reporting on the results with gas injection, and *ii*) to determine any influence that variation in the dissolved as content may have on the cavity dynamics. The physical reasoning that prompts the exploration of *ii)* is given below. Dissolved gas within the water channel can influence the freestream nuclei population as discussed in Ceccio & Brennen (1991). In addition, dissolved gas within the bulk flow gas can be exchanged with a partial cavity, as discussed recently by Lee *et al.* (2016). Typically, the liquid near the cavity may be supersaturated with dissolved gas, and mass transfer will take place into the cavity at the gas-liquid cavity interface (Parkin & Ravindra, 1991) or at the interfaces of the bubbly mixture that forms the cavity (Yu & Ceccio, 1997; Lee *et al.*, 2016). The question arises as to the effect that such gas diffusion may have on the gross dynamics of a shedding cavity, mainly in the context of changing the behavior of the bubbly flow, and this will be discussed here.

3.1 The Flow Cycle of the Shedding Cavity

For the nominal flow condition of $\sigma_0 = 2.0$ and $U_0 = 8$ ms^{-1} we observe a periodically shedding cavity, as shown in time-series recorded with visible light shown in figure 2 and with X-ray in figure 3. The top and side views with visible light were recorded simultaneously, and the X-ray data was recorded at a different time. While the conditions were nominally the same for data (from high-speed recordings) shown in figures 2 and 3, limitations in repeatability of conditions and cycle-to-cycle variations, discussed in section 3.3, cause a minor, but noticeable, discrepancy when comparing data from different shedding cycles. The sharp discontinuity in void fraction (*i.e.* the bubbly shock front) can be readily observed in figure 3, and the nature of this flow feature was extensively discussed in Ganesh *et al.* (2016). In summary, a cavity shedding cycle occurs when the separated flow region formed at the wedge apex fills with a bubbly mixture as vapor is produced near the suction peak at the wedge apex. As the void fraction of the vapor-liquid mixture within cavity increases, the sound speed of the mixture decreases to values much lower than that of either the liquid or vapor alone. With a reduction in cavitation number, the Mach number (*i.e.* the ratio of the speed of flow to local speed of sound) of the bubbly flow becomes supersonic, leading to the formation of a well-defined condensation shock front that propagates upstream with a speed (as measured in the laboratory frame) on the order of half the freestream speed. When this front impinges on the region of cavity detachment, a large-scale cloud of vapor it shed and convects downstream. Then, the growth cycle begins anew. A similar condensation shock was recently observed also by Wu *et al.* (2017), whose test section geometry and flow conditions lend the presence of the shock to also be inferable from the visible light high-speed video.

3.2 Cavity Length and Thickness

Ganesh *et al.* (2016) reported the average length and thickness of the partial cavities as a function of cavitation number. Additional measurements were conducted in the present study to determine the sensitivity of the cavity geometry to the freestream dissolved oxygen (DO) content. Figure 4a and 4b presents the cavity length and thickness based on time-averaged 10% void fraction contour, $L_{C10\%}$ and $T_{C10\%}$., respectively. As noted for figure 4(a), for $\sigma_0 < 2$ the cavity grew outside the region imaged and only thickness could be directly measured. Hence, based on data of cavity thickness-to-length ratio for $\sigma_0 < 2$, in the rest of this paper it is assumed $L_{C10\%} \sim 7.6\, T_{C10\%}$. Data are presented for DO > 50% (65 or 75%), DO ~ 50%, and DO < 50% (30 or 32%). The error bars signify the measurement. For cavitation number, as noted in section 2, propagation of uncertainty for measured quantities alone suggests usage of ±0.01 may be appropriate. However, due to observed variability in parameters measured during the experiments, a more conservative ±0.03 was taken to be the uncertainty of the cavitation number. Based on the spatial resolution of the X-ray measurements (nominally 1 mm), potential smearing of cavity closure caused by non-parallel beam paths (Mäkiharju *et al.* 2013b), sensitivity over average cavity dimensions to which segment of data was used, and erring on the conservative side, 5 mm and 2 mm were taken to be the uncertainties in cavity length and height based on average 10% void fraction contour. In all cases, the variation of cavity dimensions with respect to the dissolved gas content are small, and generally fall within the uncertainty bounds of the data.

3.3 The Natural Vapor Production Rate

With measurements of time-series of void fraction, we can determine the time evolution of the spanwise-averaged volume of vapor, $V_{gas}(t)$, in any region of interest for the strongly shedding condition, and use it to determine the volumetric vapor production rate $Q_V = dV_{gas}(t)/dt$. The cavity growth takes place in approximately 10^{-2} s, and we can measure the overall vapor production rate by taking differences in our 1 kHz time-series of void fraction images. For simplicity, we will assume that during the initial cavity growth the production rate of vapor significantly exceeds the condensation rate, as pressure in region near suction peak is near vapor pressure, and that there is negligible advection of vapor out of the control volume, as no significant outflow of gas is observable in visible light or X-ray. Note the rectangular control volume ("region of interest", ROI) around the cavity defined in figure 5a. We will also consider ROI's that are defined by boundary of the time-average void fraction (*e.g.* α > 5%) in the analysis below.

Figure 5b shows the average void fraction within a control volume, and the average void fraction, α, rises and falls during the shedding cycle. Two curves are shown here, with the first presenting the void fraction in the rectangular ROI, and the second showing the void fraction defined by a ROI enclosing the region of the cavity with mean void fraction greater than 5%. The trends for both curves are similar, but the peak void fractions are, of course, larger for the smaller control volume defined by the α > 5% curve. Figure 5c presents the total gas volume, V_{gas}, which is nearly insensitive to the choice of control volume since both enclose the bulk of the vapor.

The first time-derivative of the vapor volume can now be used to compute the volumetric vapor production rate, Q_V. The average maximum (*i.e.* average of all peaks detected in the recording) vapor production rate during the cavity growth, $Q_{V,max}$, is approximately 1.7 x10^{-3} m^3s^{-1} as seen in figure 6. An algorithm utilizing the frequencies based on the dynamic pressure transducer and void fraction data was utilized to automatically identify the peaks (which are numbered in the figure) associated with each cycle. We can note that even in this nominally periodic case, there is significant cycle-to-cycle variation that may be due to both the underlying shedding process, which is also highly three-dimensional as evidenced by figure 2, and variation in the freestream conditions. We have characterized the uncertainty in the incoming freestream speed and pressure, and these may be sufficient to produce some variation in the behavior of the cavitation. Also, as reported by Duttweiler and Brennen (2002), the presence of shedding partial cavitation can interact with the acoustic modes and compliance of a water tunnel, and lead to coupled behavior. And, such interactions are difficult to manage in a recirculating water channel.

Interestingly, the observed minor cycle-to-cycle variation caused 'smearing' in simply phase-averaged data (included in the supplemental on-line material), and the smeared time-series often resembled more what one would expect to see in a cycle with a re-entrant jet. A re-entrant jet would appear smeared as the vapor along most of the cavity height would not condense while a thin liquid jet travels upstream underneath the cavity. The distinction of re-entrant jet and condensation shock was further discussed by the authors in Ganesh *et al.* (2016).

We can examine the vapor production rates for a range of cavitation numbers and dissolved oxygen contents, and the data are presented in figure 7. $Q_{V,max}$ is, as it was in figure 6, the average peak vapor production rate, if we assume negligible condensation or advection during the vapor production portion of the cavity filling cycle. As shown in figure 7a, $Q_{V,max}$ increases with decreasing cavitation number, as does the cavity length. Following Stutz & Reboud (1997), we can define the flow coefficient of vapor

$$C_{V,max} = \frac{Q_{V,max}}{U_0 L_{C10\%} b}, \tag{3.4}$$

where $L_{C10\%}$ is cavity length based on based on the 10% void fraction boundary as determined by the X-ray measurement, and b is the span of the model. These data are shown in figure 7b. The normalized maximum flow coefficient ranges from $0.01 < C_{V,max} < 0.04$. Any influence of the dissolved air content is not readily discernable from the data. We can also note that the time-averaged normalized vapor production rate when defined as in Stutz & Rebound (1997), and taking velocity profile to be same as in that reference, was found to be $\overline{C_V} \sim 0.01$, which is similar to the values reported by Stutz & Rebound (1997) based on optical bubble probe measurement.

3.4 Bubbly Shock Speed

The void fraction discontinuity (*i.e.* bubbly shock speed in most cases), U_{FL}, is the speed measured in the tangential directions along the wedge surface taken with respect to the laboratory frame of reference. U_{FL} / U_0 was determined based on the slope of the (space-time) *s-t* diagram generated by plotting the void fraction at $n = 2$ mm (*i.e.* 2 mm away from the surface), as shown in figure 8. Owing to variability from cycle-to-cycle, as well as measurement uncertainty arising from determination of the slope itself, the measured shock speed had measurable variability amongst cycles at the same flow conditions. These data were used to compute the speed of the front in the laboratory frame, and the data are presented in figure 9 as a function of the cavitation number. The uncertainty in cavitation number is determined as discussed in connection to figure 4, and vertical error bars were used to show the standard deviation of measured shock speed. The values and trends are similar to those reported by Ganesh *et al.* (2016). As in the case for the cavity geometry and vapor production rate, changes in the dissolved oxygen content did not affect the observed shock speed within the uncertainty of the data.

3.5 Void Fraction Upstream and Downstream of the Bubbly Shock

The values of void fraction upstream of the shock, α_1, are taken to be same as void fraction in the "core" of the cavity, α_{core}, and are shown in figure 10 as a function of the cavitation number. Value of α_{core} is defined based on the highest nominally uniform void fraction region, such as observable in figure 8b immediately below the black line showing the slope that indicates shock speed and also see clearly to the right of the shock in the 5th frame of figure 3. As could have been expected, the void fraction in the cavity sharply decreases as the cavitation number is increased. Also, as could be found for example from figure 8b, and similarly to figure 30 of Ganesh *et al.* (2016), the void fraction after the shock for all conditions was approximately a constant $\alpha_2 \approx 0.22$. Again, changes in the dissolved oxygen content did not alter the upstream volume fraction.

3.6 Cavity Shedding Frequency

The cavity shedding frequency could be determined based on fast Fourier transform of data from one of the two dynamic pressure transducers, or based on void fraction data. Frequencies

based on each were generally found to agree, and as the dynamic pressure transducers had higher temporal sampling frequency, for the rest of the paper we base the shedding frequency, *f*, on the upstream dynamic pressure transducer data, $p_{d1}(t)$. Figure 11a shows the measured frequencies. The Strouhal number based on cavity length (assuming $L_{C10\%} \sim 7.6\ T_{C10\%}$ as discussed in Section 3.2) is defined as

$$St = \frac{f L_{C10\%}}{U_0} \tag{3.4}$$

As shown in figure 11b, the Strouhal number was found to be ~0.28 and exhibited no significant dependence on the dissolved oxygen contents of the water.

4. Effect of Gas Injection on Cavity Topology, Void Fraction and Vapor Production Rate

As we discuss the results of gas injection into the cavity, it is useful to compare the injected gas volume flux to the volumetric rate of water vapor production for the natural cavity. We will again focus on the baseline shedding condition of $\sigma_0 = 2.0$ and $U_0 = 8$ ms^{-1}. For this case the average peak vapor production rate $Q_{V,max} = 1.7 \pm 0.5$ x10^{-3} m^{3}s^{-1}. We can compare this vapor production rate with the volume flux of the injected non-condensable gas, Q_I, where the volume flux is computed for a given injected gas mass flux assuming that the gas is at the average temperature and pressure (~5 kPa) of the cavity flow. In the present experiments, the injection rate was varied to span $0.01 < Q_I/Q_{V,max} < 1.2$, and this range was chosen such that the injected gas flux may interact with, but in most cases not overwhelm, the baseline natural cavity flow.

At this point, we should also evaluate whether the method by which the gas was injected is likely to significantly affect the flow. We can use a simple scaling to assess the importance of the momentum flux imparted by the injected gas by comparing the momentum flux of the gas relative to the momentum flux of the bubbly shock front. As the combined area of the gas injection holes was approximately 1.5 x10^{-5} m^2, highest mass flow rate of gas injected 2 x10^{-4} kgs^{-1} (10 slpm) and cavity pressure at apex measured on average to be as low as 5 kPa, the gas momentum flux parallel to the surface was $\dot{m}_{gas} U_{gas} cos\theta_{gas,injection} \sim 0.03$ N. We can compare this with to the momentum of the bubbly shock front if we assume that the flow has a density half that of the pure liquid and a speed of approximately 4 ms^{-1}, yielding a value of $\dot{m}_{shock} U_{shock} \sim 6$ N. Hence, the momentum of the gas injected was always less than 0.5% of the momentum of the bubbly shock front, and we can assume that the injected gas momentum flux does not play a determinative role in the cavity dynamics.

4.1 Cavity Void Fraction and Topology with Gas Injection

Figure 12 presents images of the time average (left column) and root-mean-square deviation (RMSD) (with latter multiplied by two to enable use of common colorbar) of the void fraction (right column) for minimal rates of gas injection, $0 < Q_I/Q_{V,max} < 0.16$ from the apex injector. We can observe the significant *reduction* in both time-averaged void fraction and void fractions RMSD with *increasing* minimal gas injection, with void fraction minima observed at $Q_I/Q_{V,max} \approx 0.07$. After the minima, the average void fraction begins to increase owing to volume of non-condensable gas. As the cavity with reduced condensable vapor contents is more stable, even as the average void fraction begins to increase again after the minima at $Q_I/Q_{V,max} \approx 0.07$,

the void fraction fluctuations remain significantly reduced. (Note: The local minima in void fraction, as evident in figure 12, is also evident in figure 18 discussed later.)

The images for mid-cavity injection are shown in figure 13 for minimal gas injection with $0 < Q_I/Q_{V,max} < 0.16$. Here, the effect of the gas injection is much less pronounced. Then, with further increases in gas injection flux $Q_I/Q_{V,max}$ up to 1.20, as shown in figure 14, where the first two rows show results from repeating conditions shown by first and last rows of figure 13. At the highest injected gas flux the gas fills the region from injector to apex, and a gas jet emanating from the apex is observed. In is interesting to note that the region of the suction peak near the apex becomes filled with gas, and at the highest injection rates remains constantly filled as evident by dramatic drop in the void fraction RMSD in the suction peak region seen in the last two rows. *I.e.* locally the void fraction RMSD drops as some regions remain filled with gas and the flow no longer has a clear shedding cycle. And, the shedding cycle gradually becomes harder to define as $Q_I/Q_{V,max}$ exceeds 0.48.By the time $Q_I/Q_{V,max}$reached 1.20, no clearly discernable cycle can be observed). At the highest gas injection rates, the volume of the injected non-condensable gas surpasses that of the vapor, as expected.

The movies showing sample datasets, some corresponding to cases from figures 12 through 14, accompanying this paper (available at the Journal of Fluid Mechanics website) further shed light on how the changes in average and RMSD void fraction manifest in the dynamics of the cavity.

4.2 Influence of Gas Injection on Averaged Void Fraction and Vapor Production Rate

Here we will first focus on cases of limited gas injection, where $Q_I/Q_{V,max} < 0.16$. Figure 15a presents the time-averaged void fraction distribution with outlines shown for the rectangular and 5% time-averaged void fraction contour ROIs for apex injection at two gas fluxes of $Q_I/Q_{V,max}$= 0.07 (figure 15a-c) and 0.16 (figure 15d-f). Compared to figure 5 we see that apex injection leads to a *decrease* in the cavity gas volume for increasing $Q_I/Q_{V,max}$ *up to a point*, as well as a remarkable reduction in the unsteadiness. $Q_I/Q_{V,max}$ ~ 0.07 was the gas flux that led to the largest reduction in the average void fraction, as the non-condensable gas flux was sufficient to reduce vapor production, but not a significant contribution to it. The physical explanation for the decreased cavity gas volume and reduction in unsteadiness is that gas injection altered the cavity flow in two basic ways. First, injection of gas could suppress the formation of vapor. And this effect is pronounced for injection at the apex, where the injected gas would increase the local pressure in the suction peak region and could also alter the turbulent flow of the separating shear layer. Secondly, after vapor condenses more remains of bubbles containing non-condensable gas. Both of these can contribute to decrease in unsteadiness.

Figure 16 presents similar data for two cases of mid-cavity injection, with $Q_I/Q_{V,max}$= 0.07 (figure 16a-c) and 0.16 (figure 16d-f). Again, compared to figure 5 the shedding cycle appears perturbed (*i.e.* it tends to be more irregular than without gas injection), and from this data it appears limited injection into the cavity produces an initial decrease in the total volume, but then an increase at higher injected fluxes, as also evident from later discussion and data shown in figure 18.

The normalized maximum gas production rate during injection, $C_{V,max}$ determined in the rectangular control volume is shown in figure 17 for increasing $Q_I/Q_{V,max}$. (Compare to figures 6 and 7.) Note here that measured gas production rate is a combination of both water vaporization and non-condensable gas injection. Given that the non-condensable gas is injected

steadily, we do not expect that the limited introduction of gas would modify the peak *rate* of gas production during a shedding cycle. Yet, the data suggest that limited gas injection does lead to a *suppression* of the peak gas production rate as evident from reduction in average peak vapor production rate. Also, the standard deviation (signified by the vertical error bars) is noticeably reduced for $Q_I/Q_{V,max} >$ ~0.05. And, the reduction in average peak production rate is more significant for the case of gas injection from the apex.

The suppression of the gas production rate can be illustrated in another way by examining the amount of gas within the ROI for varying $Q_I/Q_{V,max}$. If the ROI is a fixed control volume, and the mean flow is in equilibrium, we can assume that flux of non-condensable gas injected into the cavity will be equal to the flux at exit. If we assume that the average velocity of the exiting gas is a fraction of the freestream velocity, κU_O, (κ= 0.5) and density of gas based on pressure averaged between apex and downstream pressure taps, then the volume balance in a ROI that encloses the mean cavity yields the following relationship between the volume of injected gas in the ROI, V_I, as a function of the volumetric injection rate, Q_I, with normalization based on the natural vapor production rate:

$$V_I = \frac{Q_I L_{ROI}}{\kappa U_0} \tag{4.1}$$

where L_{ROI} is the length of the region of interest over which volume is measured, and through which gas is assumed to move through at average velocity of κU_0. This mass balance does not include the natural vapor production, so we can use it to compare the measured amount of vapor to the amount we would expect just from injection alone. Figure 18 plots the measured volume of gas, V_{gas}, and scaled injected volume, V_I, as a function of $Q_I/Q_{V,max}$. At the low values of $Q_I/Q_{V,max}$, natural vapor production dominates. However, as $Q_I/Q_{V,max} \rightarrow 1$ and beyond, the volume of the injected gas begins to comprise the majority of the gas in the cavity.

Examining time-series of spanwise averaged void fraction distribution (void fraction movies provided in supplementary on-line material), the influence of the gas injection location on cavity fluctuations can be more drastic than is made clear from previous figures. If we seek to define a single parameter that better captures the suppression of fluctuations, we can define the time average of the gas volume when the instantaneous void fraction is between chosen low (L) and high (H) threshold values α_L and α_H

$$\overline{V_{[\alpha_L,\alpha_H]}} = \frac{1}{T}\int_0^T V(\alpha_L < \alpha < \alpha_H, t)\, dt \tag{4.2}$$

Comparing this quantity with two sets of thresholds, α_{L1} and α_{H1}, *versus* two different thresholds, α_{L2} and α_{H2}, we can scale the volume fraction fluctuations as $\overline{V_{[\alpha_{L1},\alpha_{H1}]}}/\overline{V_{[\alpha_{L2},\alpha_{H2}]}}$. To avoid averaging over incomplete shedding cycles, T is taken to be the cycle time multiplied by the largest integral multiple of full shedding cycles in the recorded data set. The data are presented in figure 19 for α_{L1} = 50%, α_{H1} = 60%, α_{L2} = 20%, and, α_{H2} = 30% for the apex and mid-cavity injection. The chosen threshold values provide a clear distinction between cases that based of video seen by a human observer are easy to label as distinct. However, within a range O(10%), other threshold values would also enabled similar distinction to be made.. The ratio for mid-cavity injection falls from ~0.25 to ~0.10 with increasing gas injection, and this indicates that the relative periods of higher gas volume are reduced. The influence of apex injection is even more drastic, as increasing gas flux drives the relative period of high gas volume to almost zero.

4.3 Effect of Gas Injection on the Mean Cavity Static Pressure

Gas injection directly influences the mean static pressure in the region of flow separation (*i.e.* near the location of the suction peak) and within the cavity itself. Figure 20a presents the apex cavitation number σ_A for $0 < Q_I/Q_{V,max} < 1.2$. The data show that gas injection at the apex will roughly double σ_A from ~0.08 to ~0.17 (p_A from ~5 kPa to ~8 kPa) over the range of $0 < Q_I/Q_{V,max} < 0.2$. A similar trend is observed for injection into the cavity, although about 1.5 times gas injection volume is needed to produce the same effect. Higher gas volumes injected into the cavity lead to further increases in pressure, but the effect saturates for $Q_I/Q_{V,max} > 0.8$. This result can be contrasted with the change in the downstream cavity pressure resulting from injection at either location. Figure 20b presents σ_C for the same conditions. In this case the change is much less drastic, suggesting that the injection location in not an important factor.

Re-examining the data in figure 17, we see that at $Q_I/Q_{V,max} \sim 0.06$ for apex injection, $C_{V,max}$ has been reduced to ~0.01 from a non-injection value of ~0.03. This would correspond to an increase in the cavitation number from $\sigma_0 = 2.0$ to a value of ~2.3 for the non-injection (*e.g.* baseline) flow, if we consider the data of figure 7. The data from figure 20a suggest that injection at $Q_I/Q_{V,max} \sim 0.06$ increases the apex cavitation number by ~0.05. Thus, the increase in apex pressure due to injection can account for some of the suppression of the gas production, but not all. While the increase in mean pressure near the cavity detachment is likely to be the most *direct* effect that gas injection has on the vapor production, suppressing the liquid tension that results from the separated flow near the suction peak, the injection of gas into the turbulent shear layer may also depress the turbulent pressure fluctuations that can lead to vapor production (Gopalan & Katz 2000, Claudia & Ceccio 2002, Chang *et al.* 2011).

5. Effect of Gas Injection on the Cavity Shedding and Bubbly Shock Formation

The above data reveal that gas injection into the cavity, even for limited relative injection rates, has a demonstrable effect on the average amount of gas within the cavity and the rate at which vapor is produced during the cavity growth and shedding cycle. Such gas injection also influences the dynamic behavior of the cavity. At the baseline condition, the formation of the shock front is regular and occurs for almost every growth and shedding cycle. This cyclical regularity is somewhat reduced with mid-cavity injection at low fluxes and at high fluxes ($Q_I/Q_{V,max} \sim O(1)$) the gas overwhelms the vapor. However, with apex injection, shock formation became much more irregular and could be suppressed completely even at relatively low $Q_I/Q_{V,max} \sim O(0.05)$.

5.1 Space-Time Diagrams of the Cavity Flow with Gas Injection

Part of an approximately repeating *s-t* diagram for the non-injection cavity was presented in figure 8b, and from such diagrams we determined the bubbly shock speed and the void fraction upstream of the shock (figures 9 and 10). We can compare these data to those for two injection cases to illustrate the effect of gas injection on shock formation. Figure 21 presents the *s-t* diagram for the apex injection case $Q_I/Q_{V,max} \sim 0.07$, and figure 22 presents the *s-t* diagram for the mid-cavity injection case $Q_I/Q_{V,max} \sim 0.07$. For the case of cavity injection, the cyclic nature of the shedding is modified but still present. But, for apex injection, the strong cyclical shedding has ceased. For both injection cases, the void fraction has been *reduced* by gas injection, and

this suggests that the mechanisms responsible for vapor production are being suppressed by injection.

These same trends can be observed in the unsteady pressure measurements taken on the surface of the wedge. Figures 23, 24, and 25 correspond to the conditions shown above. Here, the upstream unsteady pressure, $p_{d1}(t)$, and $p_{d2}(t)$ are plotted in (a) and (b), and the spectrum of each are presented in (c). Limiting apex gas injection significantly reduces the amplitude of the pressure fluctuations, which is consistent with the observation of reduced void fraction fluctuations. Mid-cavity injection had less of an effect, with the cavity dynamics still present, but somewhat reduced.

5.2 Void Fraction Upstream of the Bubbly Shock

From figure 10, we have shown that the void fraction upstream of the shock front in the baseline condition varies with the cavitation number, and it ranges from $0.5 < \alpha_{core} < 0.9$. The variation of the maximum (*i.e.* core) void fraction with the surrounding pressure is an important observation, as we have shown above that the process of gas injection can significantly change the static pressure at the apex. We would expect that apex injection would lead to an increase in static pressure and, therefore a decrease in the core void fraction. And, this is the case, as shown in figure 26. The baseline (no gas injection) data from figure 10 are plotted as a function of σ_A for varying σ_0 along with the core void fraction measured during gas injection at the apex injection for fixed $\sigma_0 = 2.0$. The relationship between the core void fraction and apex pressure is similar whether apex pressure changes due to gas injection or reference pressure.

5.3 Modification of Speed of Sound of Gas Mixture with Gas Injection

The speed of sound in a bubbly mixture can be estimated form an approximate relationship derived by Brennen (2005), and subsequently experimentally confirmed by Shamshborhan *et al.* (2010). Ignoring the bubble dynamics, mass transfer and assuming a homogeneous equilibrium model, the speed of sound in a bubbly flow is given by Brennen (2005) as

$$\frac{1}{c^2} = [\rho_L(1-\alpha) + \rho_G\alpha]\left[\frac{\alpha}{kp} + \frac{1-\alpha}{\rho_L c_L^2}\right] \tag{5.1}$$

Where for water vapor the polytropic index, k, is 1.3 for an adiabatic process, and 1 for an isothermal process. For the following sections, an adiabatic process is assumed. (It can be noted that for this simple model, based data from Brennen (2005) and Shamshborhan *et al.* (2010), the difference this assumption makes for the present case is insignificant in comparison to uncertainty of the experimental data we are discussing.) As evident from Eq. 5.1, increasing the cavity mixture pressure (whether by reference pressure change or gas injection) increases the speed of sound, and it is possible conditions become less favorable for shocking, as discussed in Ganesh *et al.* (2016). Speed of sound upstream of the shock c_1 can be obtained from eq. 5.1 by using the mean cavity pressure, p_A, and the averaged void fraction upstream of the shock α_1. The variation of speed on sound of this type of bubbly mixture is shown in Figure 27. Brennen (2005), Shamsborhan *et al.* (2010), and Budich *et al.* (2016) present a useful discussion concerning the different approaches that can be used to determine the speed of sound in a bubbly

mixture, including the "frozen" model used here, compared to the "equilibrium" model that can allow for phase transition.

5.4 Modification of the Bubbly Shock Propagation with Gas Injection

Ganesh *et al.* (2016) also discussed how a simple model for the shock speed is useful in interpreting the observed results. Again, ignoring the effects of bubble dynamics and assuming an isothermal flow, we may develop the following relationship for the expected propagation speed of the condensation front

$$U_1^2 = \frac{p_2 - p_1}{\rho} \frac{(1-\alpha_2)}{(1-\alpha_1)(\alpha_1-\alpha_2)} \tag{5.2}$$

where α_1 and p_1 and α_2 and p_2 are the void fraction and static pressures upstream and downstream of the front, taking as $\alpha_1 \approx \alpha_{core}$ that was given in figure 10. We will similarly assume that $U_1 \approx U_{FL}$, the discontinuity front speed measured with X-ray visualization in the laboratory frame of reference. (At higher gas fluxes, based on observed dynamics we refer to a discontinuity front to be more general, as this may no longer be a shock.) The void fraction discontinuity propagation speed U_{FL} / U_0 is shown in figure 28 as a function of $Q_I/Q_{V,max}$. For both apex and mid-cavity gas injection, the introduction of non-condensable gas reduced the observed discontinuity front speed.

We can use the relationship between the expected shock speed (equation 5.2), pressure and void fraction to discern how gas injection can modify the shock speed, and perhaps eventually eliminate shocks. There are two primary mechanisms through which injection can have an effect. First, the injection of gas will change the void fraction of the cavity flow; and second, gas injection will modify the local cavity pressure. The data presented above show that even limited gas injection can decrease the core void fraction and increase the cavity pressure.

A decrease in the pressure difference across the shock will decrease the shock speed. However, examination of equation 5.2 indicates that the shock speed may be reduced *or* increased through modification of the maximum void fraction within the cavity. Setting the derivative of equation 5.2 with respect to cavity void fraction upstream of the shock, $(\partial U_1/\partial \alpha_1)$, equal to zero, we define the critical void fraction $\alpha_{1,cr} = (1+\alpha_2)/2$. When $\alpha_1 < \alpha_{1,cr}$, a decrease in the core void fraction upstream of the front will lead to an *increase* in the shock speed. While, with $\alpha_1 > \alpha_{1,cr}$, a decrease in the core void fraction will lead to a *decrease* shock speed. The void fraction downstream of the shock was almost constant, with $\alpha_2 \approx 0.22$. This would make $\alpha_{1,cr} \approx 0.61$. The data in figure 26 show that the void fraction upstream of the shock is typically greater than 0.6. Hence, we would expect that, all else being equal, decreases in the core void fraction would contribute to a decrease in the shock speed, which was observed.

The reduction in the core void fraction from 0.9 to 0.6 would lead to a reduction in the sound shock speed U_{FL}/U_0 by around 2/3 with all else held constant. From figure 28, we see that the shock speed has decreased by around a factor of 1/4. Therefore, we expect gas injection to decrease the pressure difference (p_2 - p_1) equal to a factor of $(3/8)^2 \approx 0.14$. A proxy for the pressure difference across the shock is the difference between the cavity and apex static pressure. Examining figure 20 and raw data, we can see that limited injection leads to a doubling of the apex pressure and a 50% increase in the cavity pressure, which would substantially reduce the pressure difference. Indeed, when $Q_I/Q_{V,max} \approx 0.2$, the pressure difference is almost eliminated.

Ganesh *et al.* (2016) showed that the measured pressure across the shock front for the baseline flow is on the order of 4 kPa. Therefore, an increase in (p_2 - p_1) of only one or two kPa would be sufficient to slow the speed of the shock, and this amount is well within the pressure rises caused by gas injection.

Based on the discontinuity propagation speeds *in the laboratory frame* shown in Figure 28, and the speed of sound upstream of the discontinuity shown in Figure 27, the Mach number of the discontinuity front propagation can be estimated, and this data is shown in Figure 29. As the injection rates increases, the void fraction discontinuity tends to propagate sub-sonically, at least in the laboratory frame. That is, if it is truly sub-sonic, it can no longer be a shock, thus supporting the interpretation of time-series recordings that the shedding mechanism may have switched to one dominated by a re-entrant jet. Furthermore, for many cycles the rollup of the vapor cavity occurred whilst propagation of a sharp thick region of condensation was not observable in the X-ray recording, which would be consistent with transition of the shedding mechanism to a re-entrant jet type.

5.5 Shedding Frequency

The introduction of gas reduced the dominant shedding frequency, *f*, as shown in Figure 30a. The Stouhal number based on the cavity length was also modified by gas injection, and this is presented in Figure 30b. Recall that the length of the cavity decreases with increasing volume flux. Therefore, *St* remains roughly constant with increasing gas flux for mid-cavity injection, even though the shedding frequency is reduced. We note that in case of the apex injection, or injection at a high gas flux $Q_I/Q_{V,max} \sim O(1)$, the cavity became only weakly periodic, and the definition of dominant frequency is not necessarily comparable to the dynamics associated with cavity shedding.

6. Conclusions

In the present work, we extend the observations of partial cavity flows reported by Ganesh *et al.* (2016). We examine how dissolved gas might influence the cavity dynamics, and we observed how limited non-condensable gas injection into the cavity could alter the cavity topology and dynamics. For the range of dissolved gas contents examined, variation of the freestream dissolved gas content (as determined based on the dissolved oxygen content) did not change any measured property of the cavity flow within the limits of our measurement uncertainty. This is not to say that freestream gas content can never play a role in partial cavity inception and dynamics. Rather, we conclude here that any mass transfer of dissolved non-condensable gas into the developed partial cavity with a strongly enforced separation line did not have any appreciable influence. This is also implied by the results of Lee *et al.* (2016), who examined diffusion into limited cavities on the same geometry. From their results, we would expect the maximum rate of gas mass diffusion into the cavity to be on the order of 10^{-6} kg s^{-1}, which would occur at the highest dissolved gas content. This would lead to a volume flow rate of $Q_{DO} \approx 2 \times 10^{-5}$ $m^3 s^{-1}$, or $Q_{DO}/Q_{V,max} \approx 10^{-2}$, which is almost an order of magnitude smaller that the limiting rates on gas injection needed to measurably influence the baseline cavity flow. We should also note that this insensitivity to water quality differs from the observation of Kawanami *et al.* (2005) who found a significant effect of spectra of the cavitation. In their study, the lack of available dissolved and free gas (nuclei) supressed the re-growth of a periodically shedding cavity forming near the leading edge of a two-dimensional hydrofoil. In the present study, the

cavity formed at the sharp separation line of the wedge apex and was accompanied by a strong suction peak. Unlike Kawanami *et al.* (2005), we did not observe a complete re-wetting of the cavitating surface during the cavity shedding cycle. This suggests that the rate of vapor production may be an important consideration when assessing the relative importance of dissolved gas content on the dynamics of partial cavitation. Similarly, the presence of many free gas nuclei can modify the boundary layers that occur on smooth flow surfaces upstream of cavity detachment, resulting in the modification or elimination of sheet cavitation, as discussed by Briançon-Marjollet *et al.* (1990) and Li & Ceccio (1996). This is another way that free gas content can alter the inception and development of sheet cavitation, but it is not applicable with the cavity forming on the wedge apex. Interestingly, numerical studies discussing similar effects of free nuclei and nucleation on hydrofoils were conducted by Ma *et al.* (2015) and Hsiao *et al.* (2017) and, as observed in present study, show relative insensitivity to free stream nuclei contents, which in present study is related to dissolved gas contents.

Injection of non-condensable gas into the cavity from both the apex and the mid-cavity did lead to significant changes in the cavity flow, even for cases of limited gas injection with $Q_I/Q_{V,max} \approx 10^{-1}$. Gas injection altered the cavity flow in two basic ways. First, injection of gas could *suppress* the formation of vapor, leading to the curious observation that the injection of gas could reduce the mean volume fraction in the cavity. This effect was most pronounced for injection at the apex, where the injected gas would increase the local pressure in the suction peak region and could alter the turbulent flow of the separating shear layer. Injection of gas at the mid-cavity also led to increases in the mean cavity pressure and a reduction in vapor production, however, to a significantly lower degree.

By altering the cavity volume fraction and pressure, gas injection led to significant changes in the overall cavity dynamics. The formation of bubbly shock waves is a fundamental process for cavity shedding of the baseline flow. Gas injection suppressed (or even eliminated) shock formation. When the shocks formed, they were often slower than the non-injection conditions. This change was related to modification of both the maximum (pre-shock) void fraction and the local cavity pressure. Therefore, these results suggest that non-condensable gas injection can supress cavity shedding that results from bubbly shock formation. This would then allow re-entrant shedding re-emerge as the dominant mechanism.

Acknowledgements

This work was sponsored by the Office of Naval Research under Grant N00014-14-1-0292, Dr. Ki-Han Kim program manager.

References

AMROMIN, E. & MINIZE, I. 2003 "Partial cavitation as drag reduction technique and problem of active flow control," *Marine Engineering*, **40**(3), 181-188.

BRENNEN, C. E. 2005 *Fundamentals of multiphase flow*. Cambridge University Press.

BRENNEN, C. E. 1995 *Cavitation and bubble dynamics*. Cambridge University Press.

BRIANÇON-MARJOLLET, L., FRANC, J.P. & MICHEL, J.M. 1990. "Transient bubbles interacting with an attached cavity and the boundary layer," *Journal of Fluid Mechanics*, **218**, 355-376.

BUDICH, B., SCHMIDT, S. J., & ADAMS, N. A. 2016 "Numerical Investigation of Condensation Shocks in Cavitating Flow," *Proc. 31st Symposium on Naval Hydrodynamics*, Monterey, California.

CECCIO, S. L., 2010 "Friction drag reduction of external flows with bubble and gas injection," *Annual Review of Fluid Mechanics*, **42**, 183-203.

CECCIO, S.L. & BRENNEN, C.E., 1991 "Observations of the dynamics and acoustics of travelling bubble cavitation," *Journal of Fluid Mechanics*, **233**, 633-660.

CHANG, N., GANESH, H., YAKUSHIJI, R., & CECCIO, S. L. 2011 "Tip vortex cavitation suppression by active mass injection. Journal of Fluids Engineering," **133**(11), 111301.

CHANSON, H. 1994 "Aeration and deaeration at bottom aeration devices on spillways," *Canadian Journal of Civil Engineering*, **21**(3), 404-409.

DUTTWEILER, M. E., & BRENNEN, C. E. (2002). Surge instability on a cavitating propeller. Journal of Fluid Mechanics, **458**, 133-152.

FRANC, J. P. & MICHEL, J. M. 2006 *Fundamentals of cavitation*. Springer Science & Business Media.

GANESH, H., MÄKIHARJU, S.A., & CECCIO, S. L. 2016 "Bubbly shock propagation as a mechanism for sheet-to-cloud transition of partial cavities," *Journal of Fluid Mechanics*, **82**, 37-78.

GOPALAN, S., & KATZ, J. 2000 "Flow structure and modeling issues in the closure region of attached cavitation." Physics of fluids, **12**(4), 895-911.

HSIAO, C-T, MA, J., & CHAHINE, G. L., 2017 "Multiscale two-phase flow modeling of sheet and cloud cavitation," Int. Journal of Multiphase Flow **90**, pp. 102-117.

IYER, C. O., & CECCIO, S. L. 2002 "The influence of developed cavitation on the flow of a turbulent shear layer." Physics of fluids, **14**(10), 3414-3431.

KARN, A., ARNDT, R. E., & HONG, J. 2016 "An experimental investigation into supercavity closure mechanisms," *Journal of Fluid Mechanics*, **789**, 259-284.

KAWAKAMI, D. T., QIN, Q., & ARNDT, R. (2005). "Water quality and the periodicity of sheet/cloud cavitation". *Proceedings of ASME 2005 Fluids Engineering Division Summer Meeting*, 513-517.

KAWAKAMI, E., & ARNDT, R. E. A. 2011 "Investigation of the behavior of ventilated supercavities," *ASME J. Fluids Engineering*, **133**(9), 091305.

LAY, K. A., YAKUSHIJI, R., MÄKIHARJU, S.A., PERLIN, M., & CECCIO, S. L. 2010 "Partial cavity drag reduction at high Reynolds numbers," *Journal of Ship Research*, **54**(2), 109-119.

LI, C. Y. & CECCIO, 1996. "Interaction of single travelling bubbles with the boundary layer and attached cavitation," *Journal of Fluid Mechanics*, **322**, 329-353.

LEE, I. H., MÄKIHARJU, S. A., GANESH, H. & CECCIO, S. L., 2016 "Scaling of gas diffusion into limited partial cavities," *Journal of Fluids Engineering*, **138**(5), 051301.

MA, J., HSIAO, C.-T., & CHAHINE, G.L., 2015 "Modelling Cavitation Flows using an Eulerianl Lagrangian Approach and Nucleation Mode"', 9th International Symposium on Cavitation, Lausanne, Switzerland, December 6th - 10th.

MÄKIHARJU, S. A., ELBING, B. R., WIGGINS, A., SCHINASI, S., VANDEN-BROECK, J. M., PERLIN, M., & CECCIO, S. L. 2013a "On the scaling of air entrainment from a ventilated partial cavity," *Journal of Fluid Mechanics*," **732**, 47-76.

MÄKIHARJU, S.A., GABILLET, C., PAIK, B.G., CHANG, N.A., PERLIN, M. & CECCIO, S.L. 2013b "Time-resolved two-dimensional X-ray densitometry of a two-phase flow downstream of a ventilated cavity," *Experiments in Fluids*, **54**(7), 1-21.

PARKIN, B. & RAVINDRA, K., 1991 "Convective gaseous diffusion in steady axisymetric cavity flows," *Journal of Fluids Engineering*, **113**(2), 285-289.

SHAMSBORHAN, H., COUTIER-DELGOSHA, O., CAIGNAERT, G., & NOUR, F. A. 2010 "Experimental determination of the speed of sound in cavitating flows," *Experiments in Fluids*, **49**(6), 1359-1373.

STUTZ, B. & LEGOUPIL, S. 2003 "X-ray measurements within unsteady cavitation," *Experiments in Fluids*, **35**(2), 130-138.

STUTZ, B. & REBOUD, J.L. 1997 "Experiments on unsteady cavitation." *Experiments in Fluids*, **22**(3), 191-198.

TOMOV, P., KHELLADI, S., RAVELET, F., SARRAF, C., BAKIR, F., & VERTENOEUIL, P. 2016 "Experimental study of aerated cavitation in a horizontal venturi nozzle," *Experimental Thermal and Fluid Science*, **70**, 85-95.

WOSNIK, M., & ARNDT, R. E. 2013 "Measurements in high void-fraction bubbly wakes created by ventilated supercavitation," *Journal of Fluids Engineering*, **135**(1), 011304.

WU, X., MAHEUX, E., & CHAHINE, G.L. 2017 "An experimental study of sheet to cloud cavitation," Experimental Thermal and Fluid Science, **83**, pp. 129–140.

YOUNG, Y. L., HARWOOD, C. M., MIGUEL MONTERO, F., WARD, J. C., & CECCIO, S. L. 2017 "Ventilation of lifting bodies: review of the physics and discussion of scaling relations," *Applied Mechanics Reviews*, **69**(1), 010801.

YU, P.W. & CECCIO, S.L., 1997 "Diffusion induced bubble populations downstream of a partial cavity," *Journal of Fluids Engineering*, **119**(4), pp.782-787.

ZVERKHOVSKYI, O. 2014 *Ship drag reduction by air cavities.* Delft University of Technology.

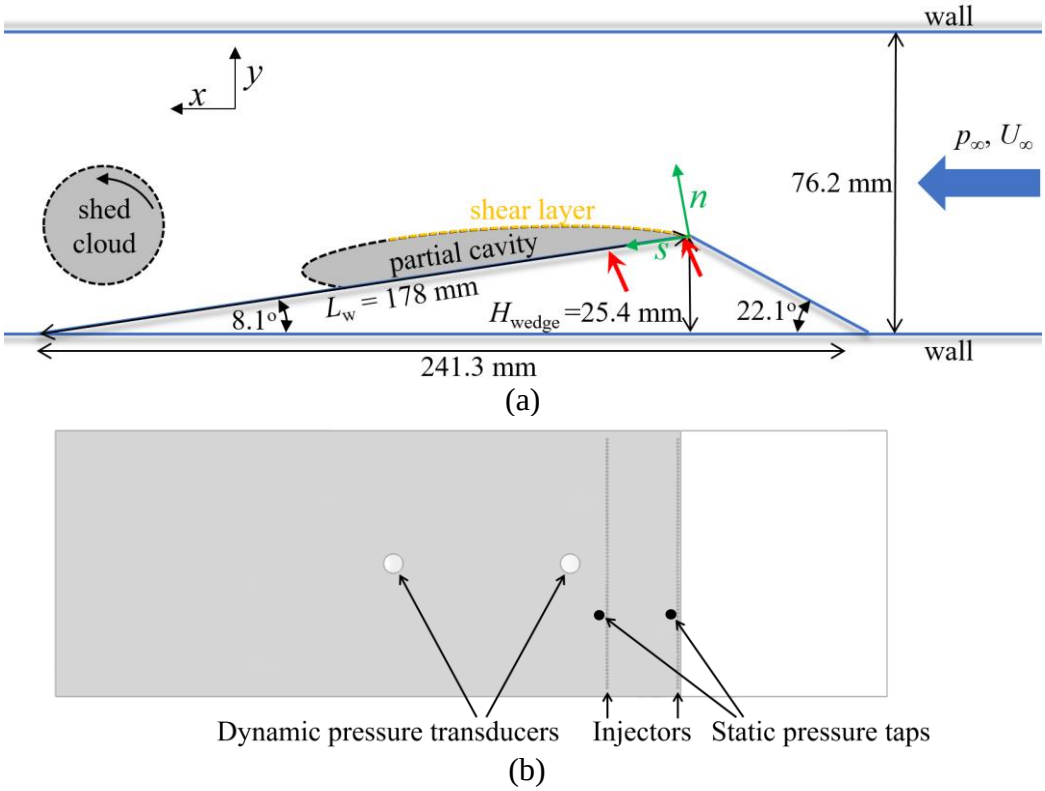

Figure 1: Schematic diagram of the cavity and experimental setup (a). Flow is from right to left, and reference pressure, p_0, and velocity, U_0, are measured 76 cm upstream of the wedge. The red arrows indicate gas injection locations. Note that the wedge apex is the origin of both *sn*- and *xy*-coordinate systems, however, the arrows indicating the orientation of the *xy*-axis are shifted for clarity. (b) wedge surface downstream of the apex as viewed along the *n*-axis showing the transducers and injector whose precise locations are given in Table 1.

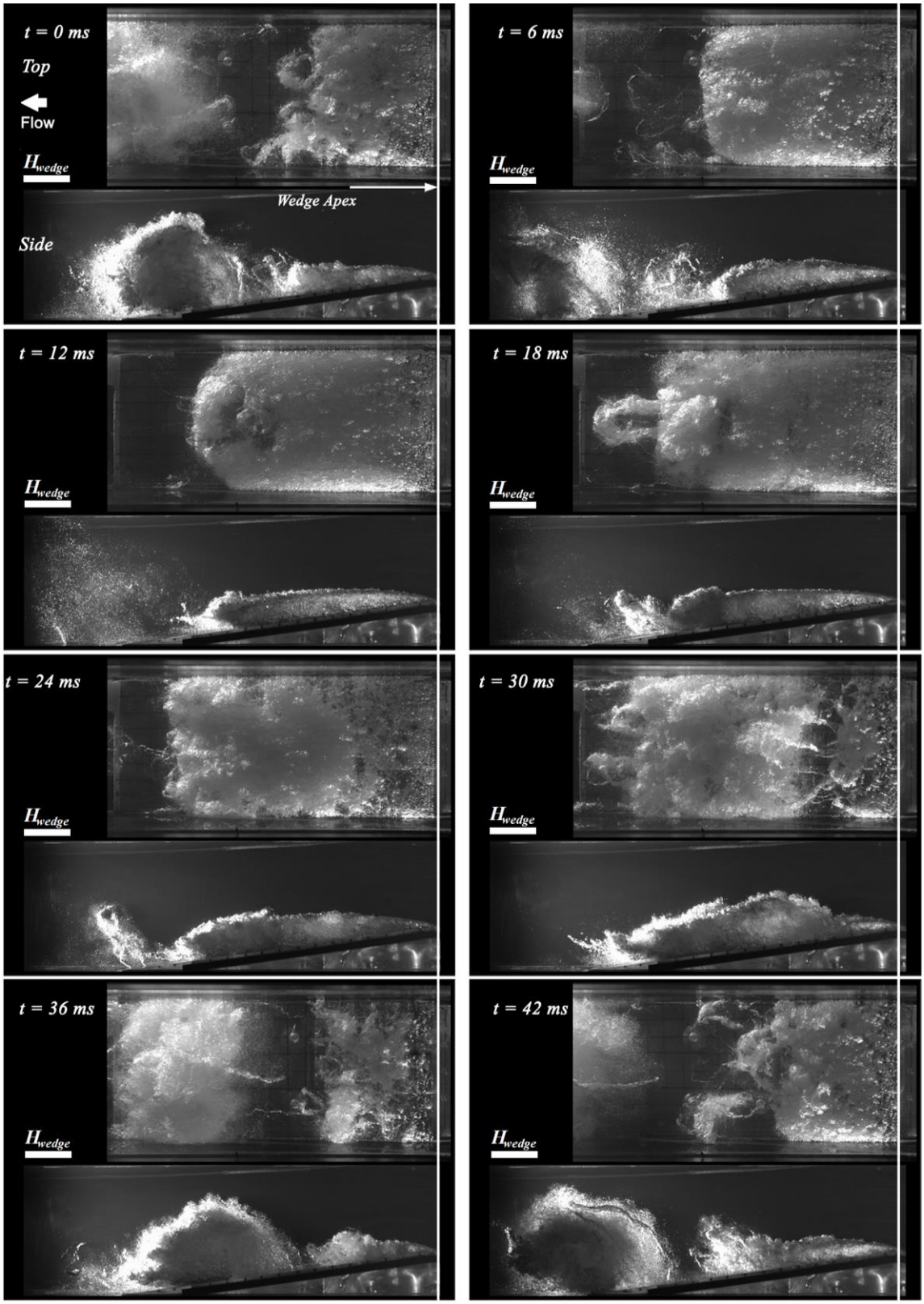

Figure 2: Top and side view time-series of the periodically shedding cavity (σ_0= 2.0 and U_0 = 8 ms^{-1}), with $t_{cycle} \approx$ 42 ms. The images show the growth, pinch-off, and shedding of a vapor cloud from the cavity near the separation line at the wedge apex. Flow is from right to left.

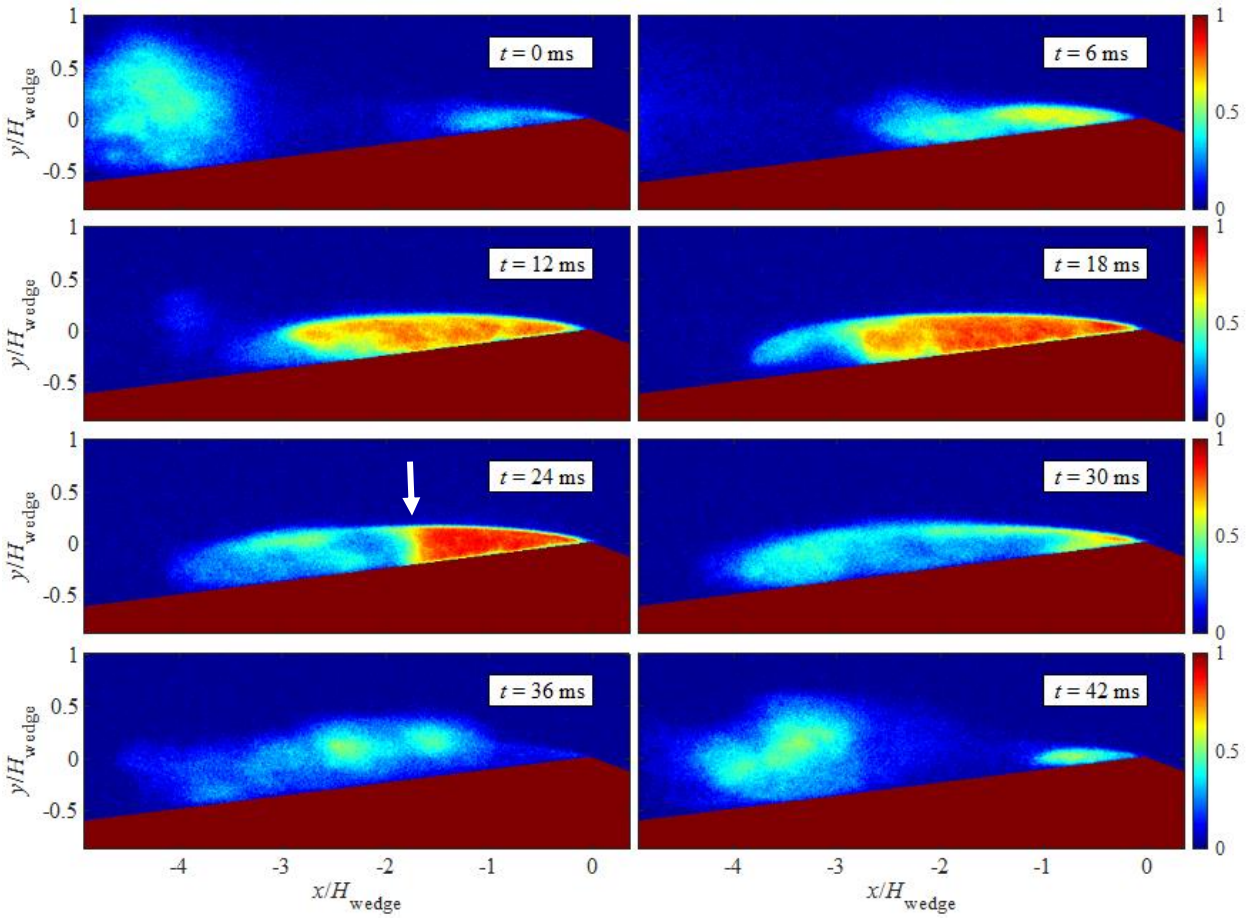

Figure 3: X-ray densitometry images showing the void fraction fields of a periodically shedding cavity ($\sigma_0 = 2.0$ and $U_0 = 8$ ms^{-1}), with $t_{cycle} \approx 42$ ms. While recorded at different times, the frames roughly match the phases of the shedding cycle shown in figure 2. The shedding results from the propagation of a void fraction discontinuity front (highlighted in the 5th frame). Flow is from right to left.

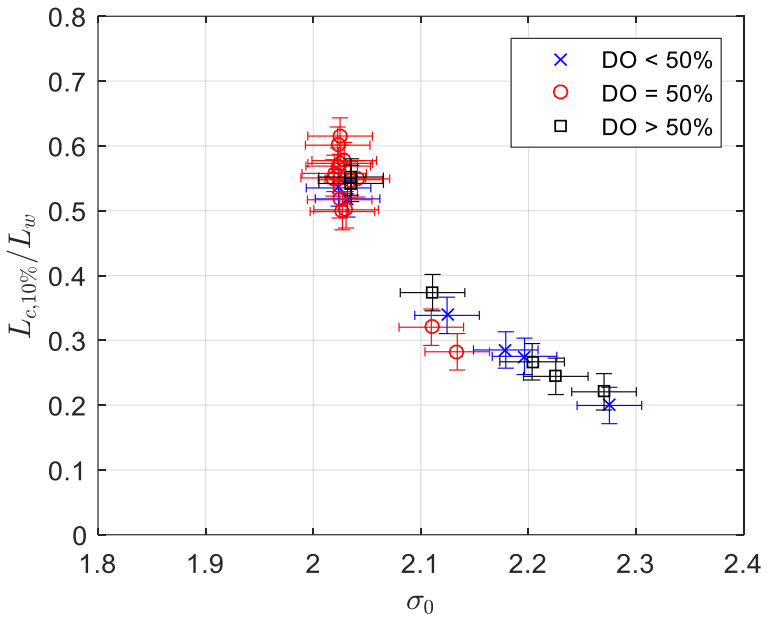

(a)

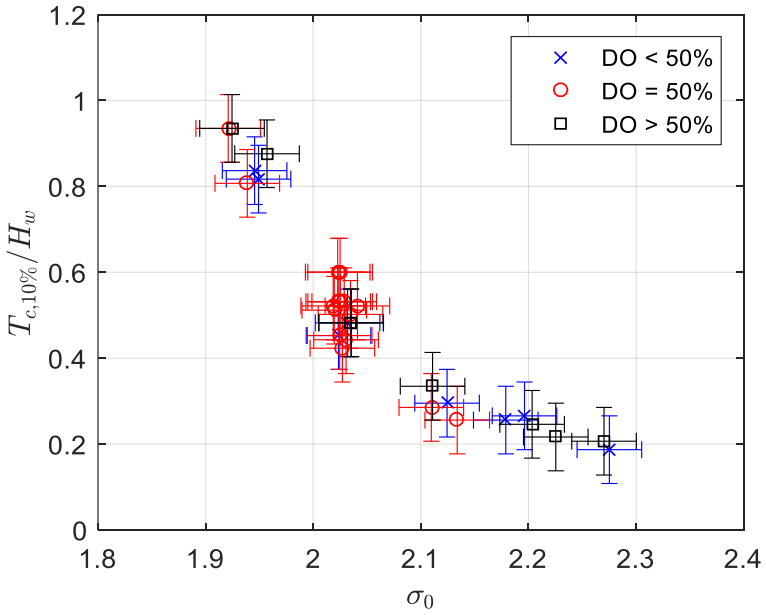

(b)

Figure 4: (a) The cavity length based on time-averaged 10% void fraction contour, $L_{C10\%}$, and (b) the maximum cavity thickness, $T_{C10\%}$, normalized by the wedge height as a function of cavitation number, σ_0. We exclude the length data where the length was near or beyond the field of view, which occurred for $\sigma_0 < 2$. The error bars signify the uncertainty described in the text.

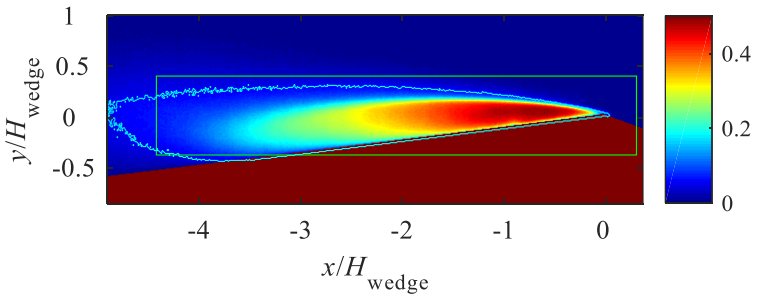

(a)

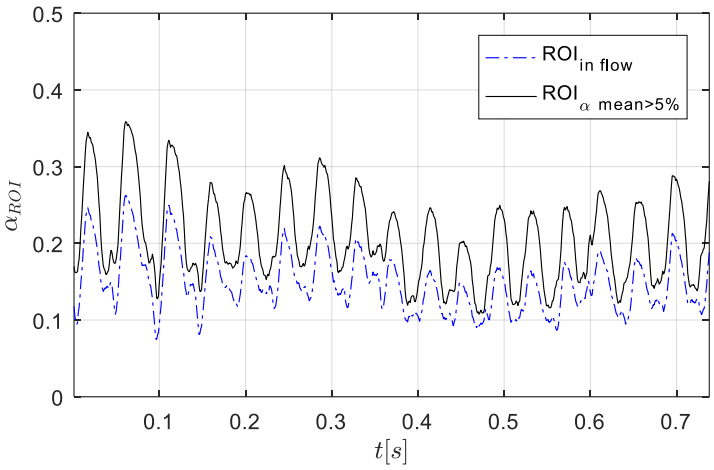

(b)

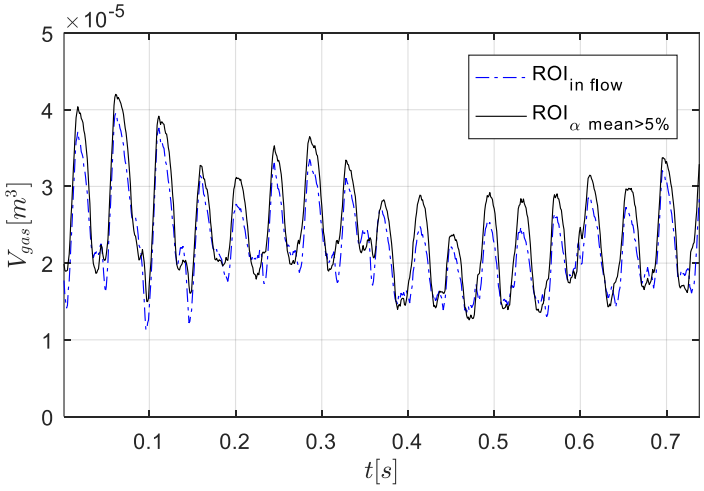

(c)

Figure 5: (a) The time-averaged void fraction distribution with outlines shown for two regions of interest (ROI); (the first ROI is rectangular and the second is based on the time-averaged 5% void fraction contour). Time-series of spatially averaged void fraction (b) and gas volume (c) within the two ROIs (outlined in (a)) for the baseline shedding cavity at $\sigma_0 = 2.0$ and $U_0 = 8$ ms^{-1}.

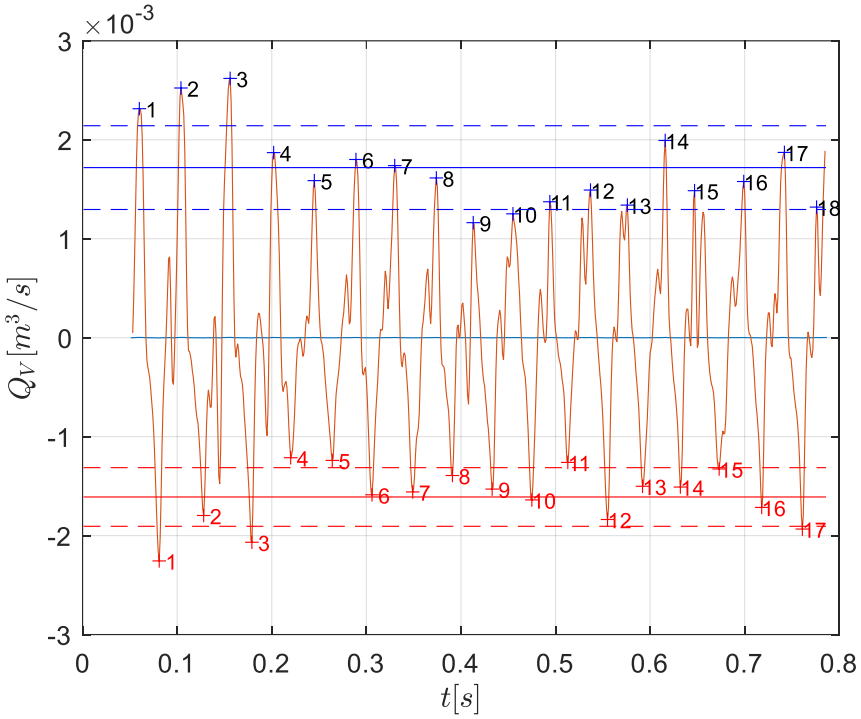

Figure 6: The vapor production rate, Q_V, as a function of time for $\sigma_0 = 2.0$ and $U_0 = 8$ ms^{-1}. The solid lines show the mean peak rates of vapor production, $Q_{V,max}$, and reduction; the dashed lines are one standard deviation away of the mean.

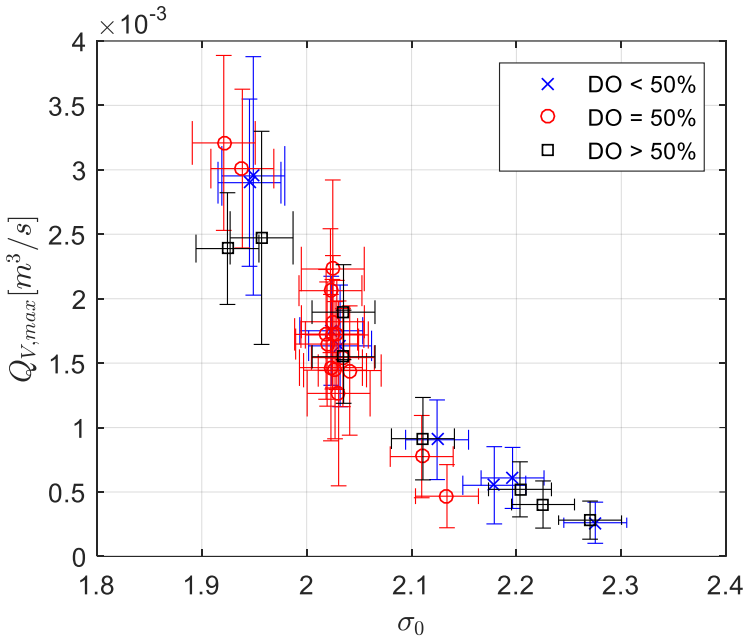

(a)

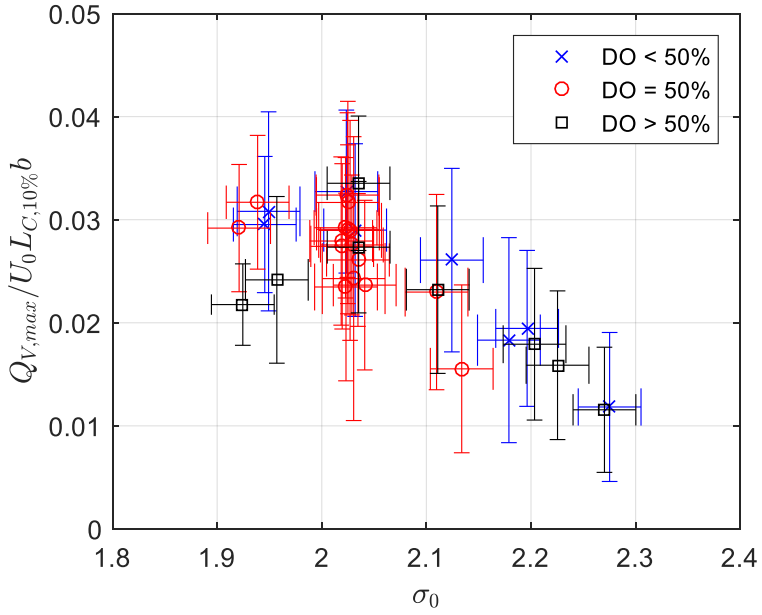

(b)

Figure 7: (a) The average maximum vapor production rate $Q_{V,max}$ as a function of σ_0; (b) the scaled flow coefficient $C_{V,max} = Q_{V,max}/U_0 L_{C10\%} b$, where the cavity length is defined by the 10% void fraction contour. U_0 = 8 ms^{-1}

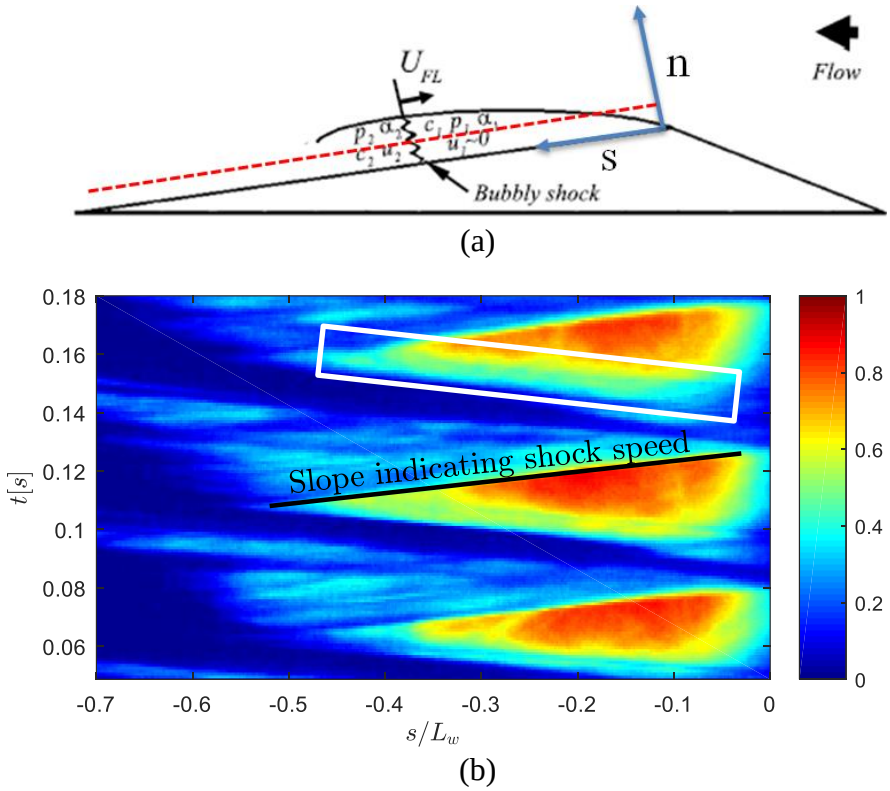

Figure 8: (a) Schematic diagram of the flow over the wedge with a red dashed line at n = 2 mm above the surface along which the void fraction was recorded; (b) the space-time (s-t) diagram of the void fraction. This diagram was used to the determination of the bubbly shock speed as described by Ganesh *et al.* (2016). The black line in the s-t diagram shows the propagation of the void fraction shock. Note the rapid cavity growth phase is discernable in this figure as the smoother discontinuity (within the white rectangle) trending up and toward the left.

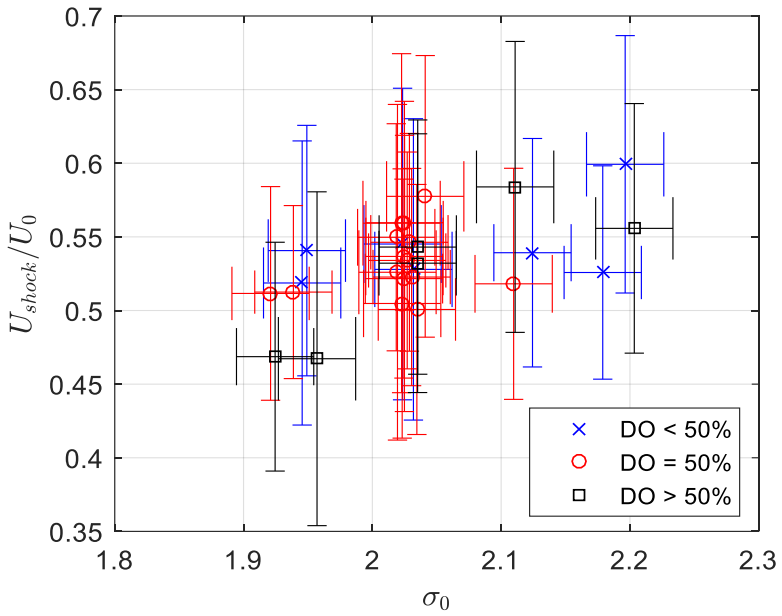

Figure 9: The propagation speed of the bubbly shock in the laboratory frame, U_{FL} / U_0, as a function of σ_0 for the non-injection conditions and with varying dissolved gas content. U_0 = 8 ms^{-1}. The horizontal error bars signify the uncertainty of cavitation number as described in the text, and the vertical error bars show the standard deviation of measured shock speeds.

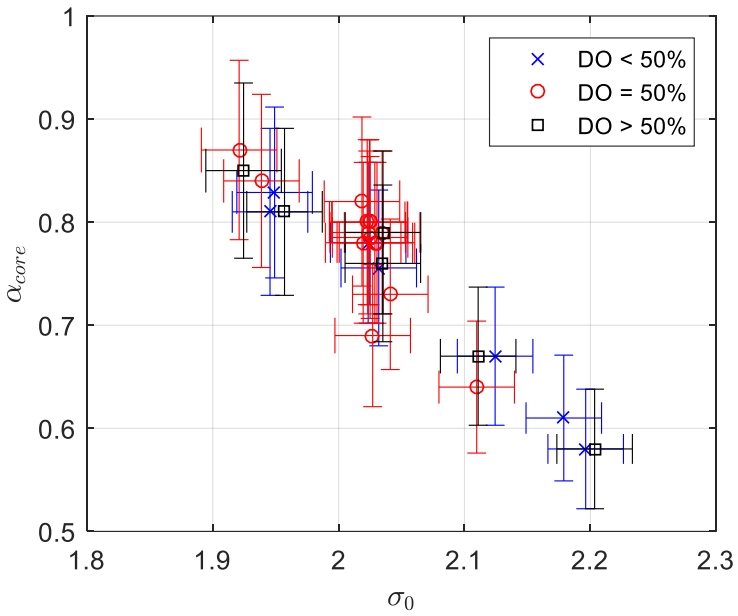

Figure 10: The void fraction upstream of the bubbly shock (at the highest nearly uniform void fraction "core" within the cavity), α_{core}, as a function of σ_0 and with varying dissolved gas content. $U_0 = 8$ ms^{-1}

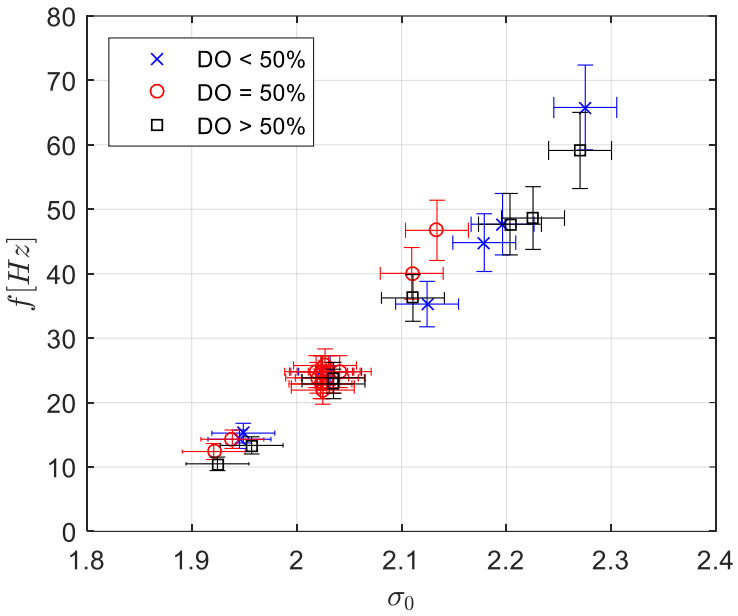

(a)

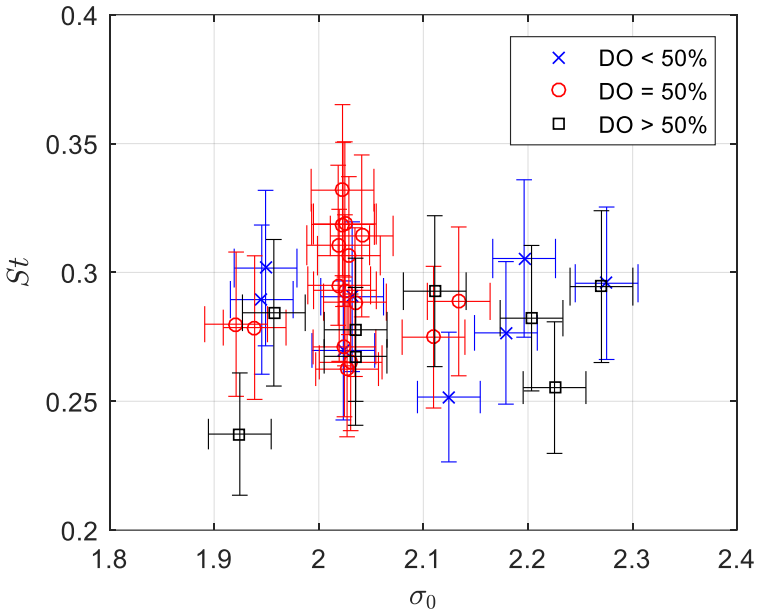

(b)

Figure 11: (a) The frequency and (b) Strouhal number, $St = fL_{C10\%}/U_0$, as a function of σ_0 and with varying dissolved gas content. $U_0 = 8$ ms^{-1}

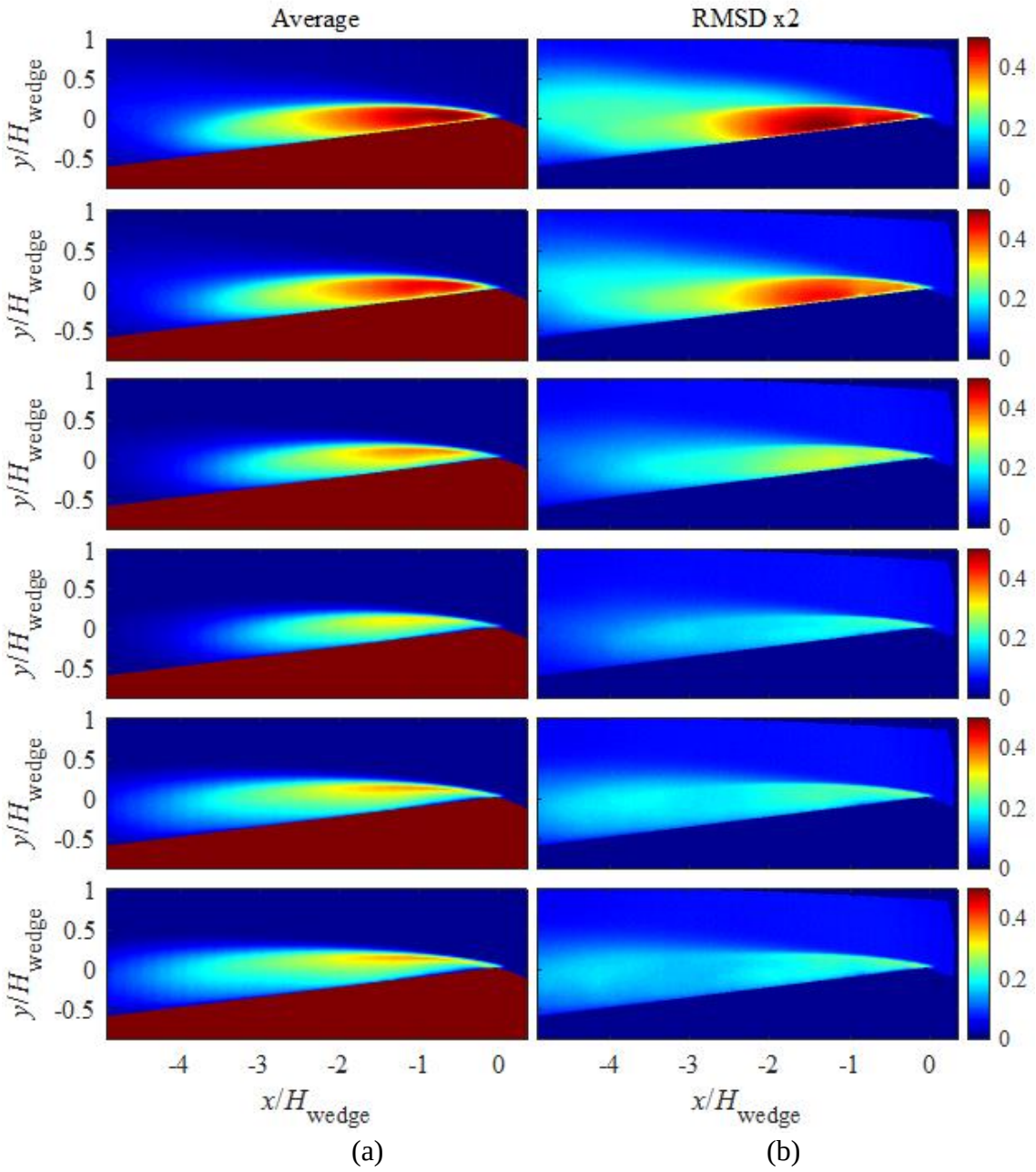

Figure 12: (a) The time-average and (b) RMSD x2 (multiplied to enable sharing color scale) of the void fraction fields for increasing rates of gas injection from the apex $Q_I/Q_{V,max}$ = 0, 0.02, 0.05, 0.07, 0.12 and 0.16 increasing from top to bottom; σ_0= 2.0 and U_0 = 8 ms^{-1}. Results from three experiments nominally at the same conditions are averaged and shown here to reduce effect cycle-to-cycle variation may have.

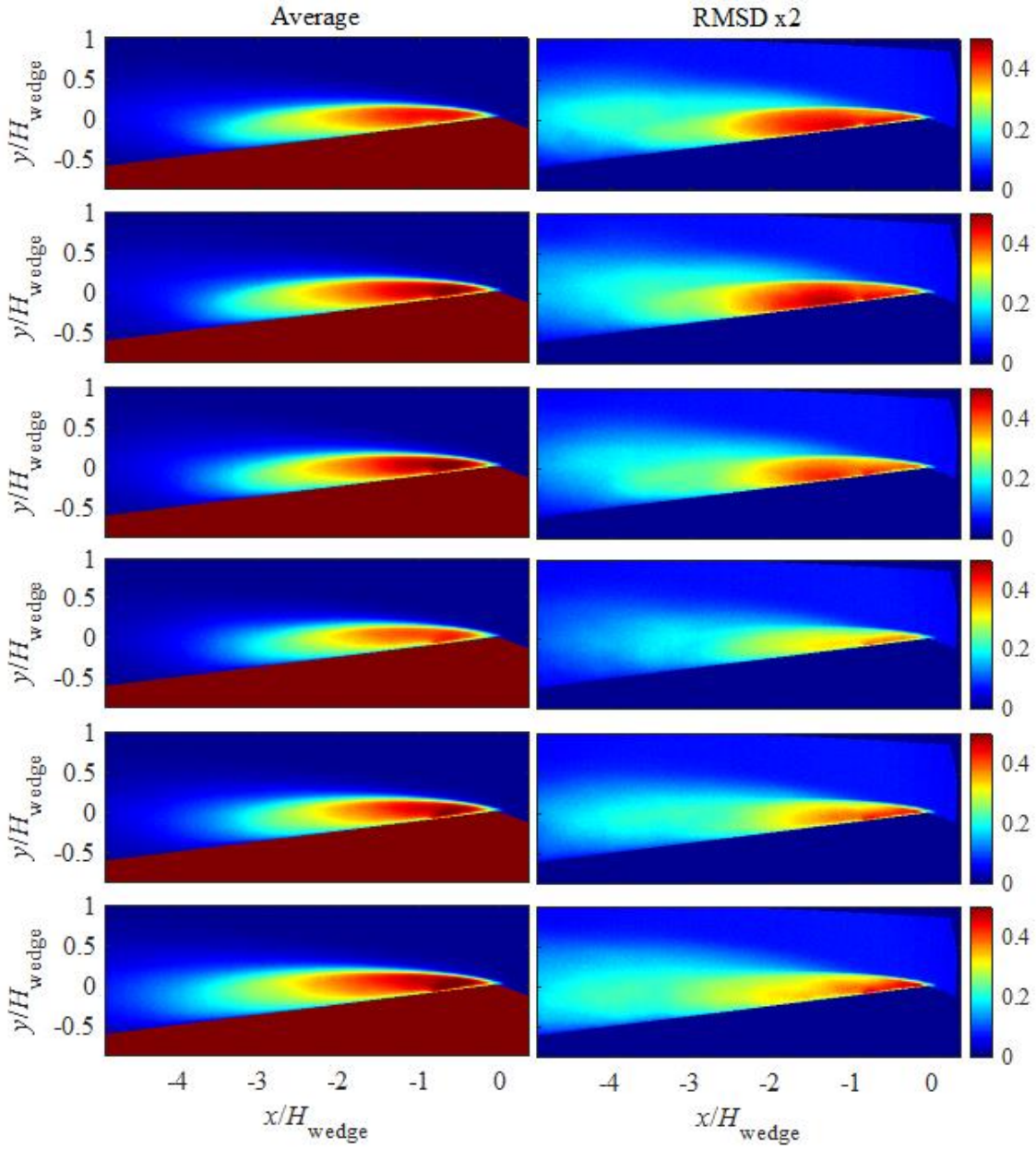

Figure 13: (a) The time-average and (b) RMSD x2 (multiplied to enable sharing color scale) of the void fraction fields for increasing rates of gas injection into the mid-cavity $Q_I/Q_{V,max}$ = 0, 0.02, 0.05, 0.07, 0.12 and 0.16 increasing from top to bottom; σ_0= 2.0 and U_0 = 8 ms^{-1}.

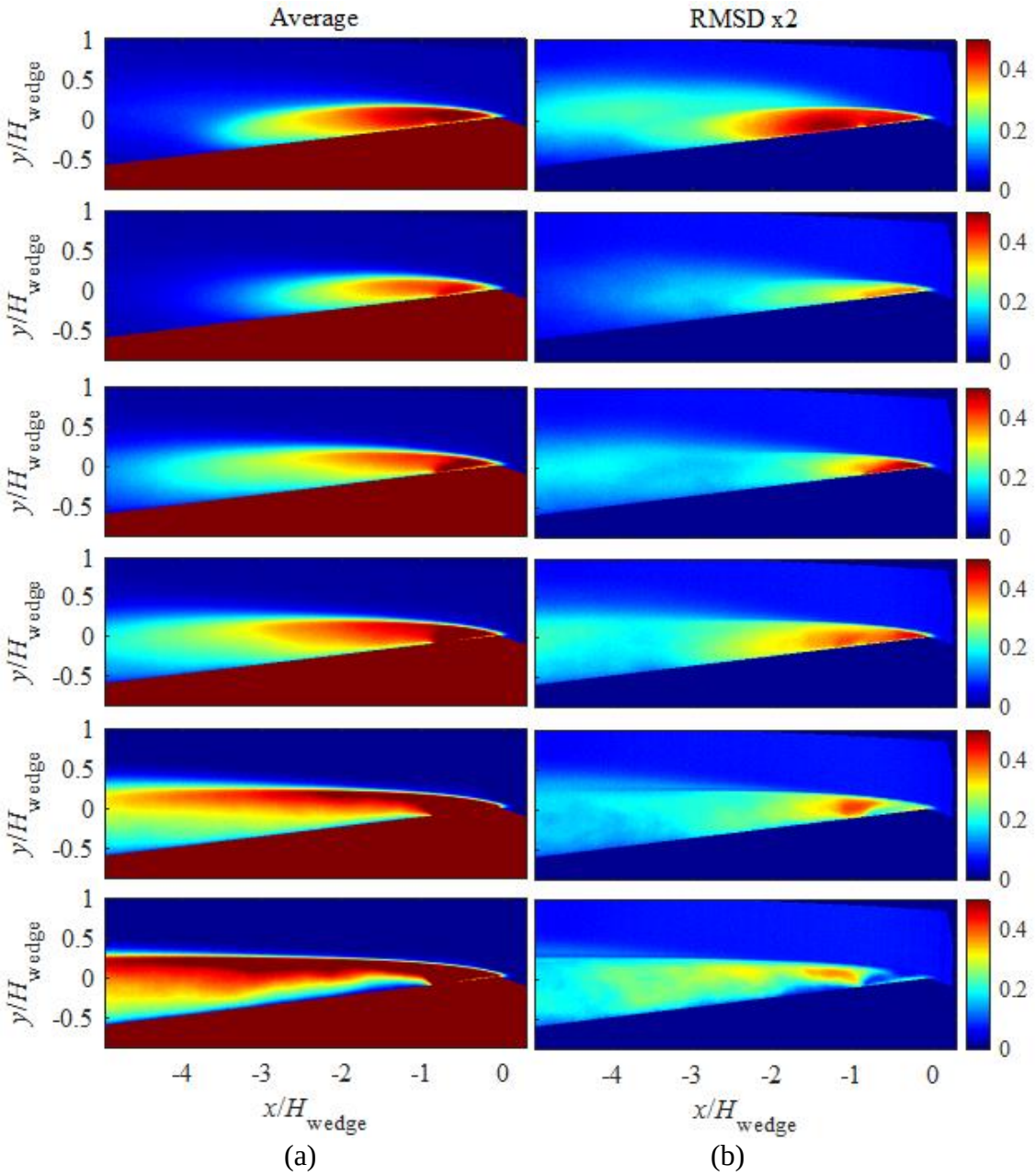

Figure 14: (a) The time-average and (b) RMSD x2 (multiplied to enable sharing color scale) of the void fraction fields for increasing rates of gas injection into the mid-cavity $Q_I/Q_{V,max}$ = 0, 0.16, 0.32, 0.48, 0.80 and 1.20 increasing from top to bottom; σ_0= 2.0 and U_0 = 8 ms^{-1}.

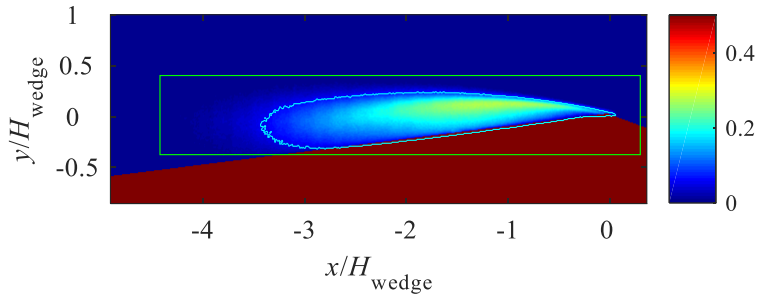
1
0.5
0
-0.5
y/H_{wedge}
-4
-3
-2
-1
0
x/H_{wedge}
0.4
0.2
0

(a)

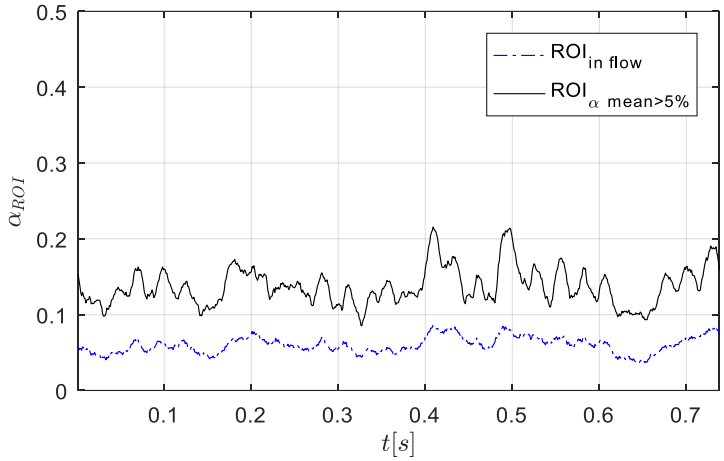
0.5
0.4
0.3
0.2
0.1
0
α_{ROI}
0.1
0.2
0.3
0.4
0.5
0.6
0.7
$t[s]$
ROI in flow
ROI α mean>5%

(b)

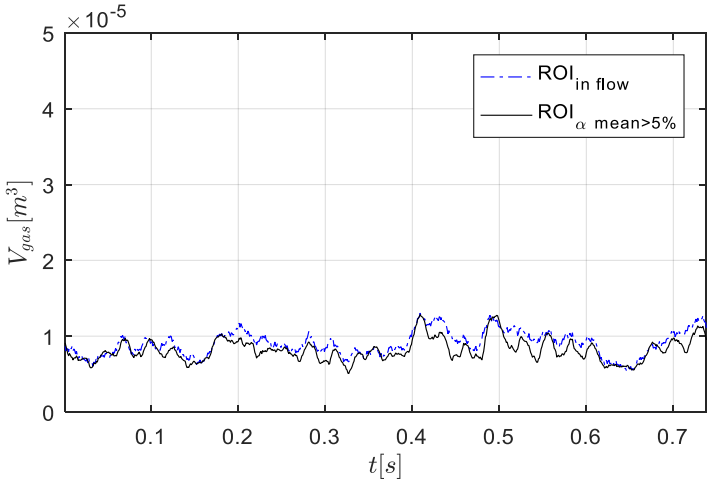
$\times 10^{-5}$
5
4
3
2
1
0
$V_{gas}[m^3]$
0.1
0.2
0.3
0.4
0.5
0.6
0.7
$t[s]$
ROI in flow
ROI α mean>5%

(c)

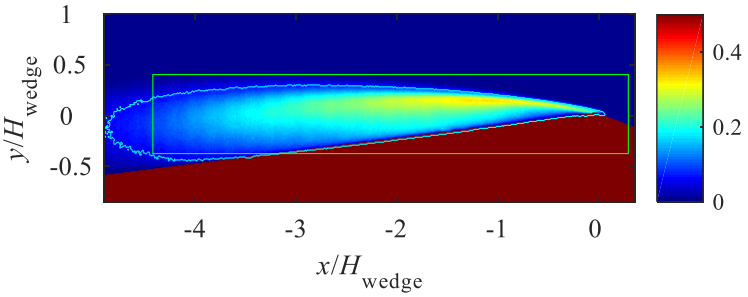

(d)

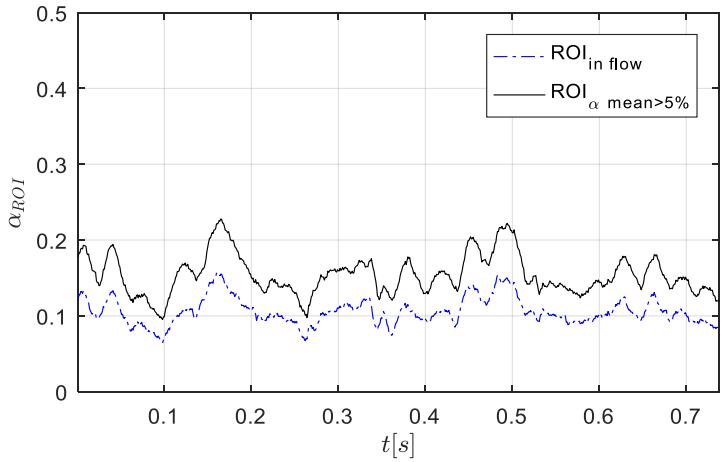

(e)

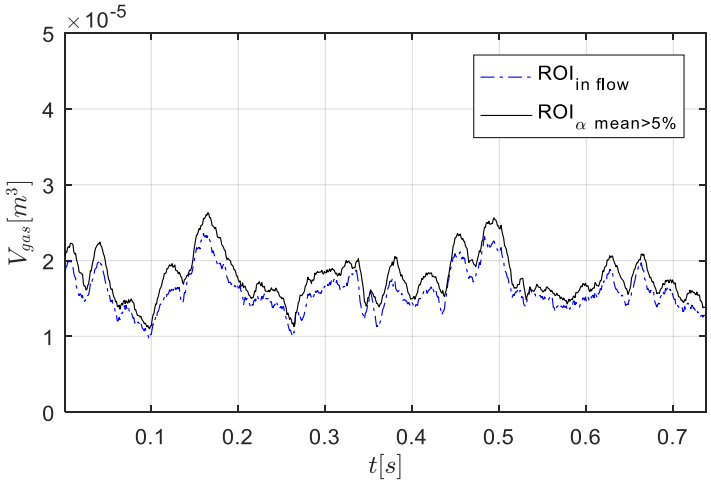

(f)

Figure 15: Apex gas injection with $Q_I/Q_{V,max}$ = 0.07 (a-c) and 0.16 (d-f); (a and d) the time-averaged void fraction distribution with outlines shown for two regions on interest (ROI); (b and e) time series of the spatially averaged void fraction and (c and f) gas volume. σ_0 = 2.0 and U_0 = 8 ms^{-1}

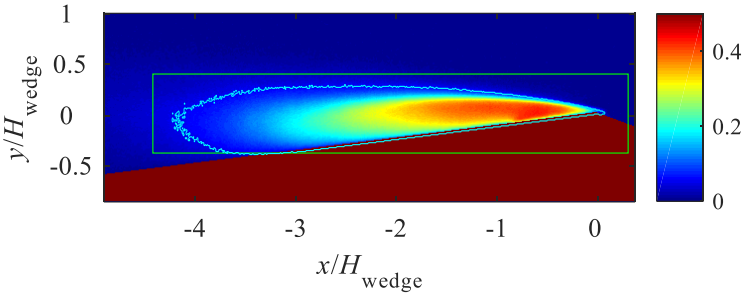
1
0.5
0
-0.5
y/H_{wedge}
-4
-3
-2
-1
0
x/H_{wedge}
0.4
0.2
0

(a)

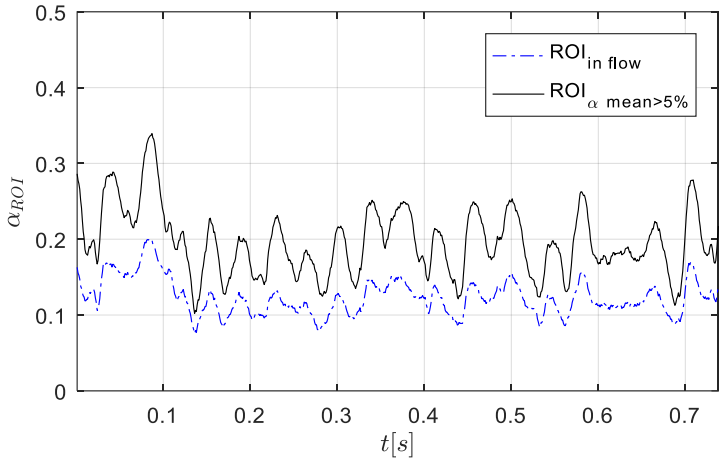
ROI in flow
ROI α mean>5%
α_{ROI}
$t[s]$

(b)

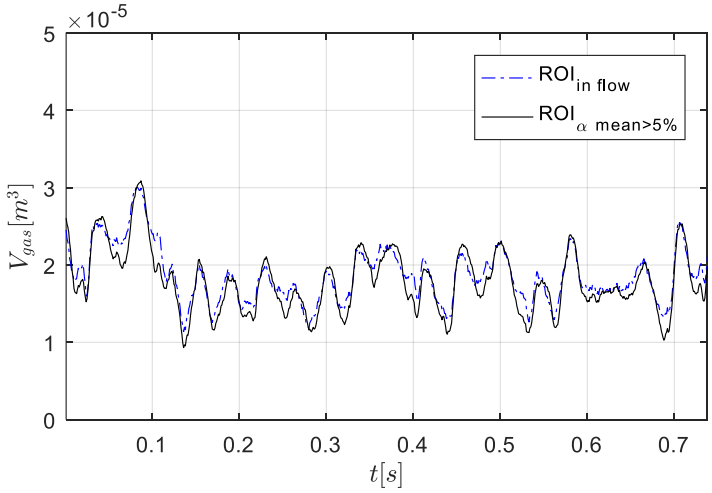
×10^-5
ROI in flow
ROI α mean>5%
$V_{gas}[m^3]$
$t[s]$

(c)

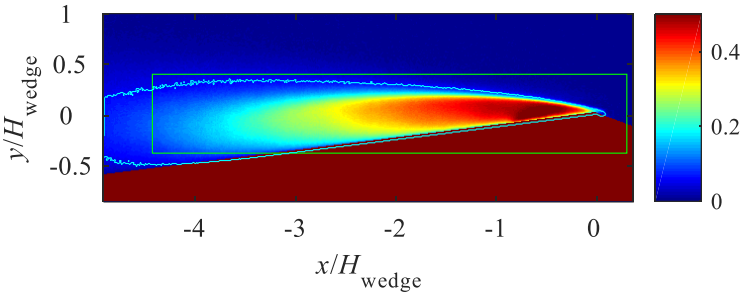

(d)

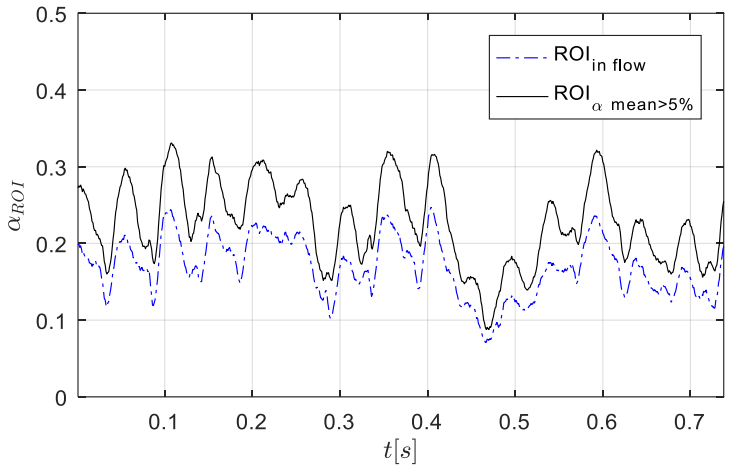

(e)

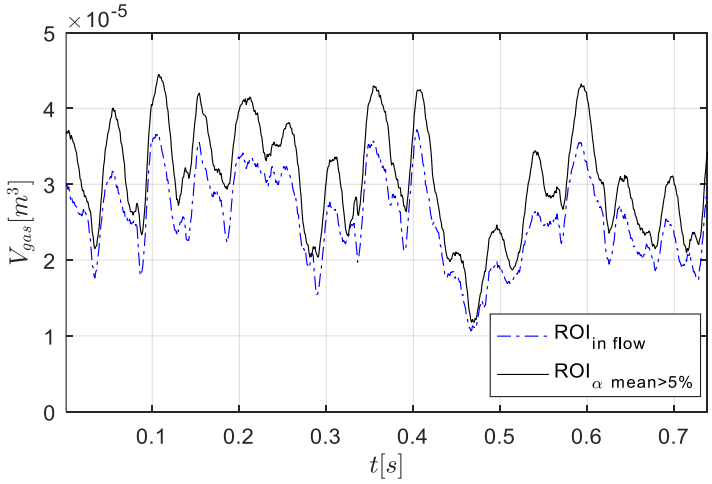

(f)

Figure 16: Cavity gas injection with $Q_I/Q_{V,max}$ = 0.07 (a-c) and 0.16 (d-f); (a and d) the time-averaged void fraction distribution with outlines shown for two regions on interest (ROI); (b and e) time series of the spatially averaged void fraction and (c and f) gas volume. σ_0 = 2.0 and U_0 = 8 ms^{-1}

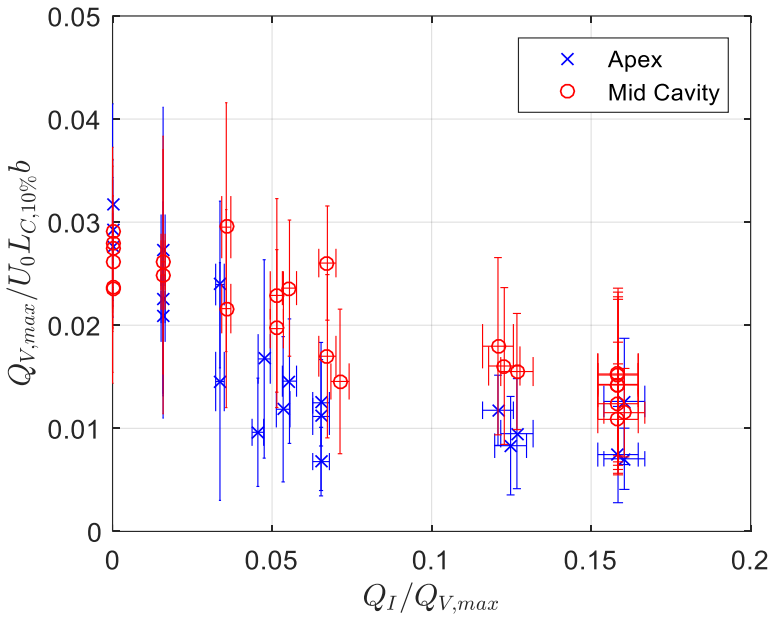

Figure 17: The average maximum vapor production rate $C_{V,max} = Q_{V,max}/U_O L_{C10\%} b$, as a function of $Q_I/Q_{V,max}$; $\sigma_0 = 2.0$ and $U_0 = 8$ ms^{-1}. The vertical bars indicate the standard deviation of the vapor production peak values.

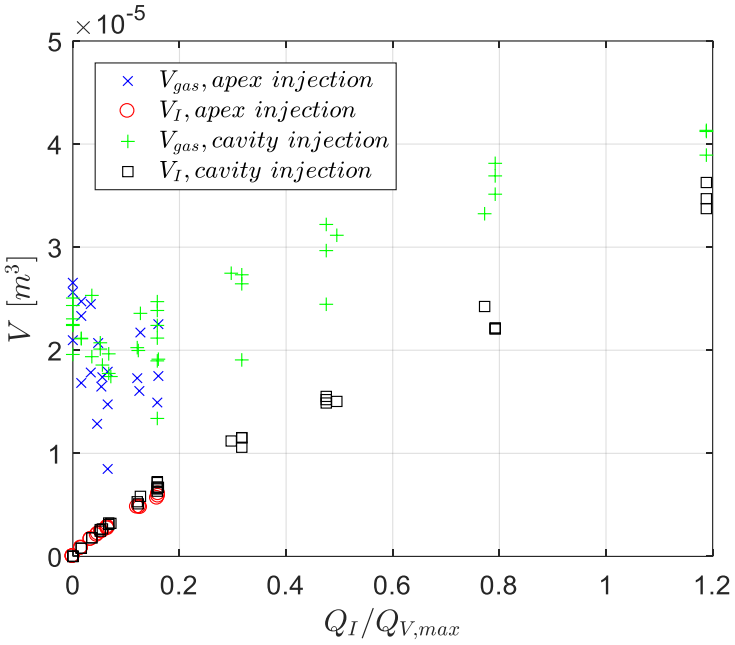

Figure 18: A plot the total gas (*i.e.* vapor and air) volume, V_{gas}, and scaled amount of injected gas (*i.e.* air) vapor $V_I = \frac{Q_I L_{ROI}}{\kappa U_0}$ as a function of $Q_I/Q_{V,max}$, where κ = 0.5. The similarity of slope between the observed and scaled injected gas volumes implies that $\kappa \approx 0.5$, *i.e.* the gas would be exiting the control volume with a speed of about half the freestream. At the low values of $Q_I/Q_{V,max}$, natural vapor production dominates. However, as $Q_I/Q_{V,max} \rightarrow 1$ and beyond, the volume of the injected gas begins to dominate the flow.
σ_0 = 2.0 and U_0 = 8 ms^{-1}

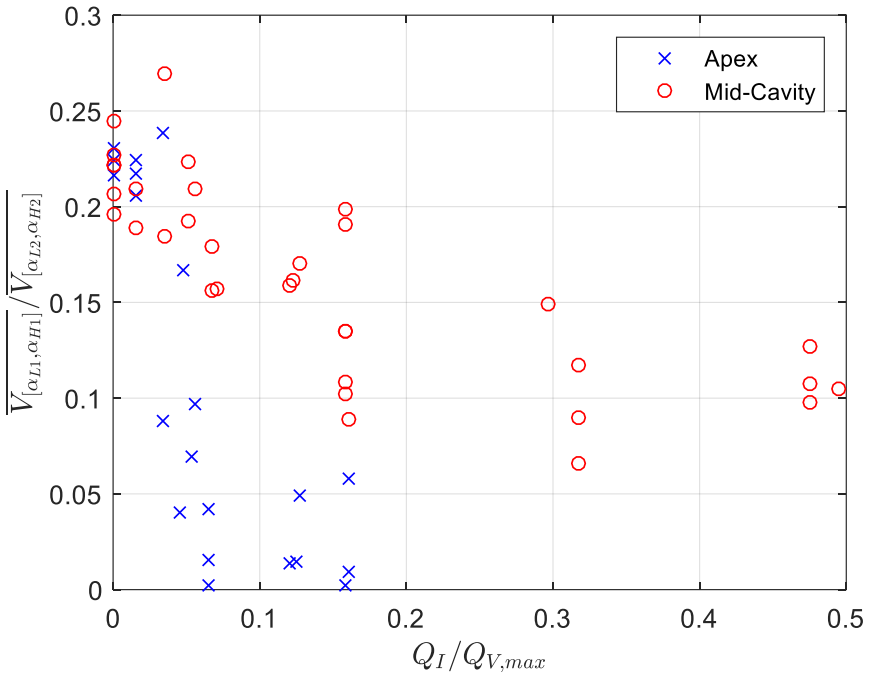

Figure 19: The scaled volume fraction fluctuations $\overline{V_{[\alpha_{L1},\alpha_{H1}]}}/\overline{V_{[\alpha_{L2},\alpha_{H2}]}}$ for α_{L1} = 50%, α_{H1} = 60%, α_{L2} = 20%, and, α_{H2} = 30% for the apex and mid-cavity injection. σ_0 = 2.0 and U_0 = 8 ms^{-1}

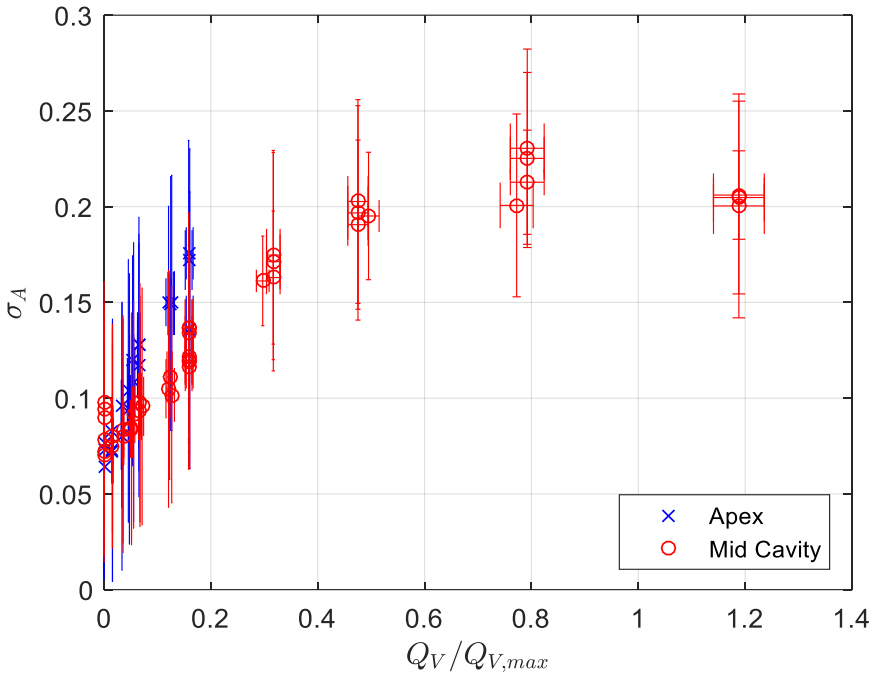

(a)

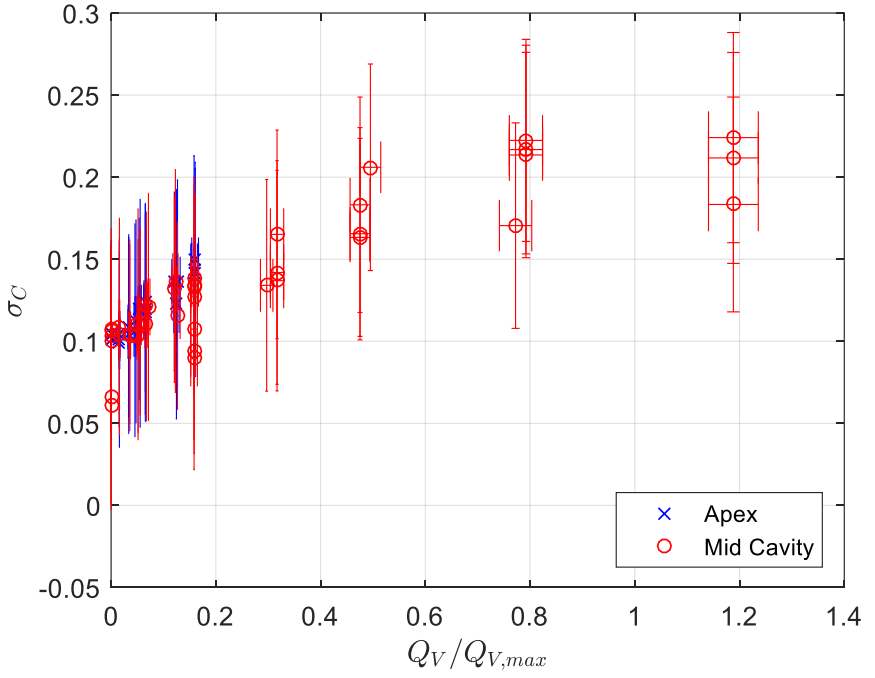

(b)

Figure 20: (a) The apex cavitation number, σ_A, and (b) the cavity cavitation number, σ_C, as a function of $Q_I/Q_{V,max}$ for apex and cavity injection. The vertical bars indicate standard deviation of the measured cavitation number; $\sigma_0 = 2.0$ and $U_0 = 8$ ms^{-1}.

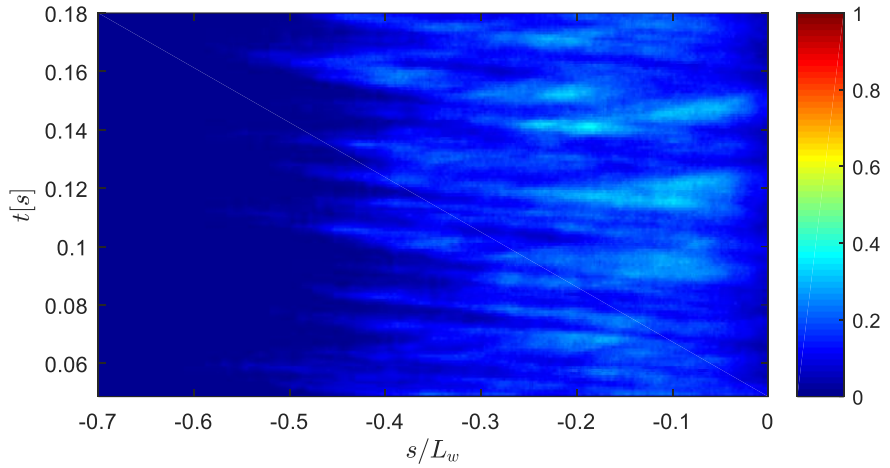

Figure 21: The *s*-*t* diagram (at n = 2 mm) for the apex injection case (same as that shown in figures 15a-c) with $Q_I/Q_{V,max}$ = 0.07, σ_0 = 2.0 and U_0 = 8 ms^{-1}. The scale bar on the right indicates void fraction and corresponding color.

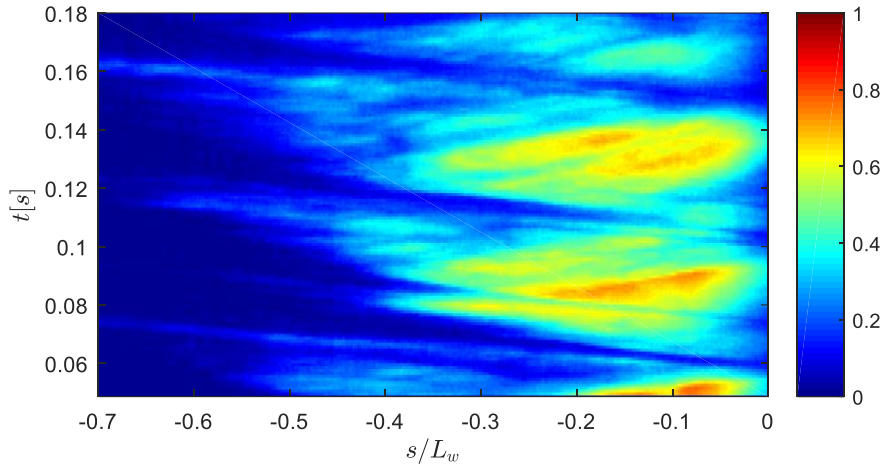

Figure 22: The *s*-*t* diagram (at n = 2 mm) for the cavity injection case (same as that shown in figures 16a-c) with $Q_I/Q_{V,max}$ = 0.07, σ_0 = 2.0 and U_0 = 8 ms^{-1}.

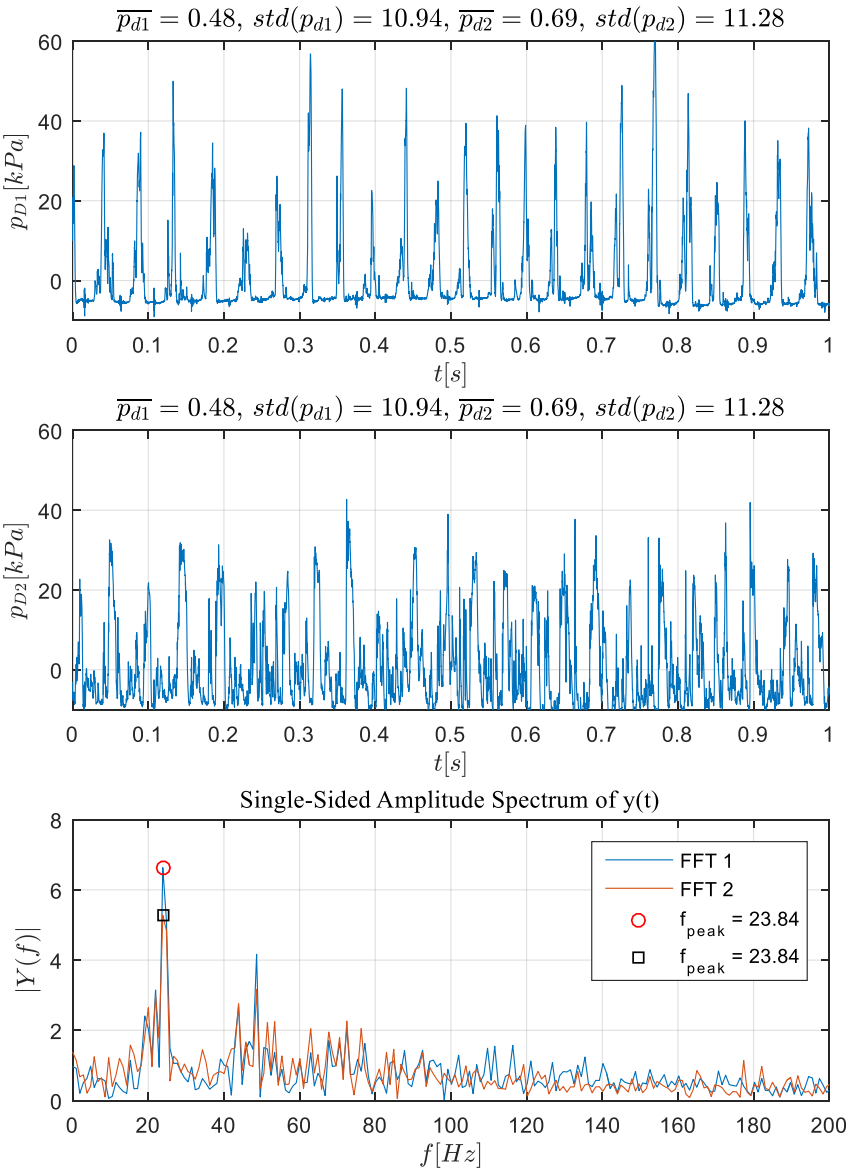

Figure 23: Time-traces of dynamic pressure at p_{d1} and p_{d2}, and their FFTs *without* gas injection. (Same case as shown in figures 5 and 8b). $Q_I/Q_{V,max}$ = 0.00, σ_0 = 2.0 and U_0 = 8 ms^{-1}. The units of averages and standard deviations listed in the titles are (kPa) and (Hz).

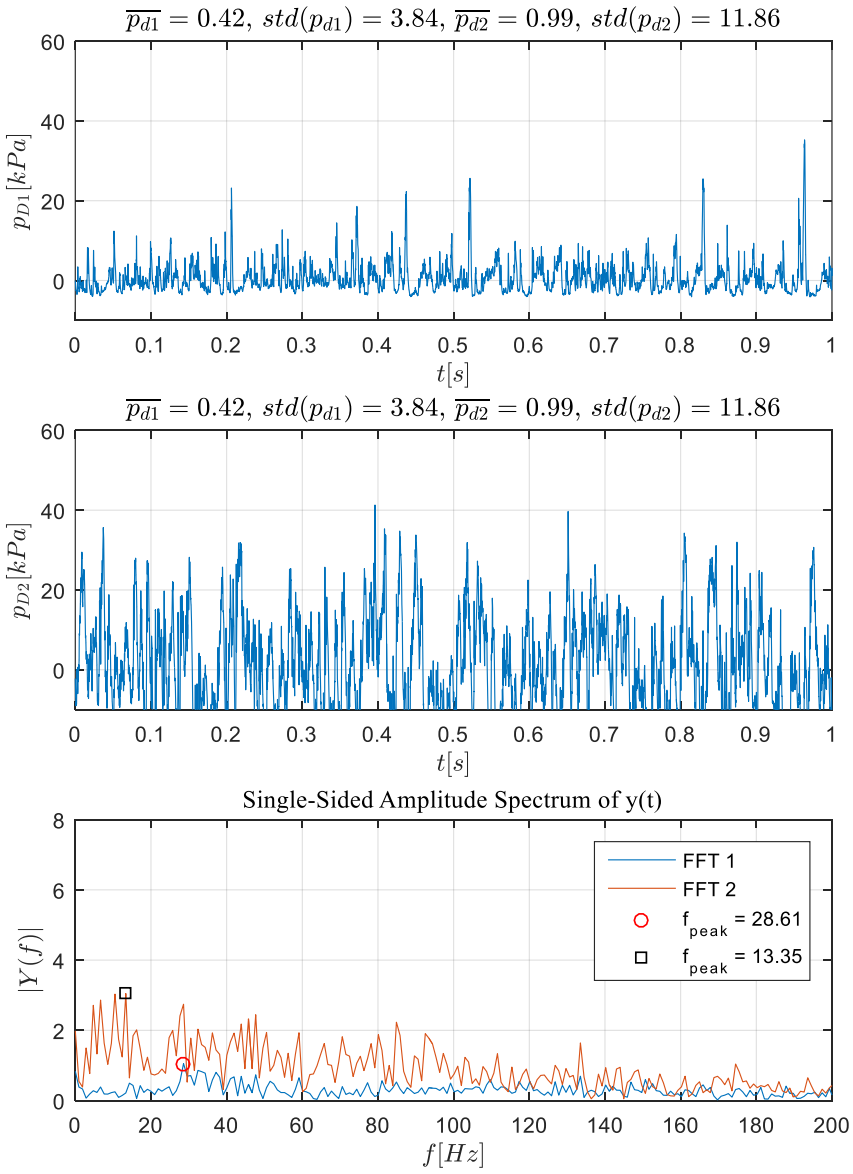

Figure 24: Time-traces of dynamic pressure at p_{d1} and p_{d2}, and their FFTs. *With apex* injection. (Same case as shown in figures 15a-c and 21). $Q_I/Q_{V,max}$ = 0.07, σ_0 = 2.0 and U_0 = 8 ms^{-1}. The units of averages and standard deviations listed in the titles are (kPa) and (Hz).

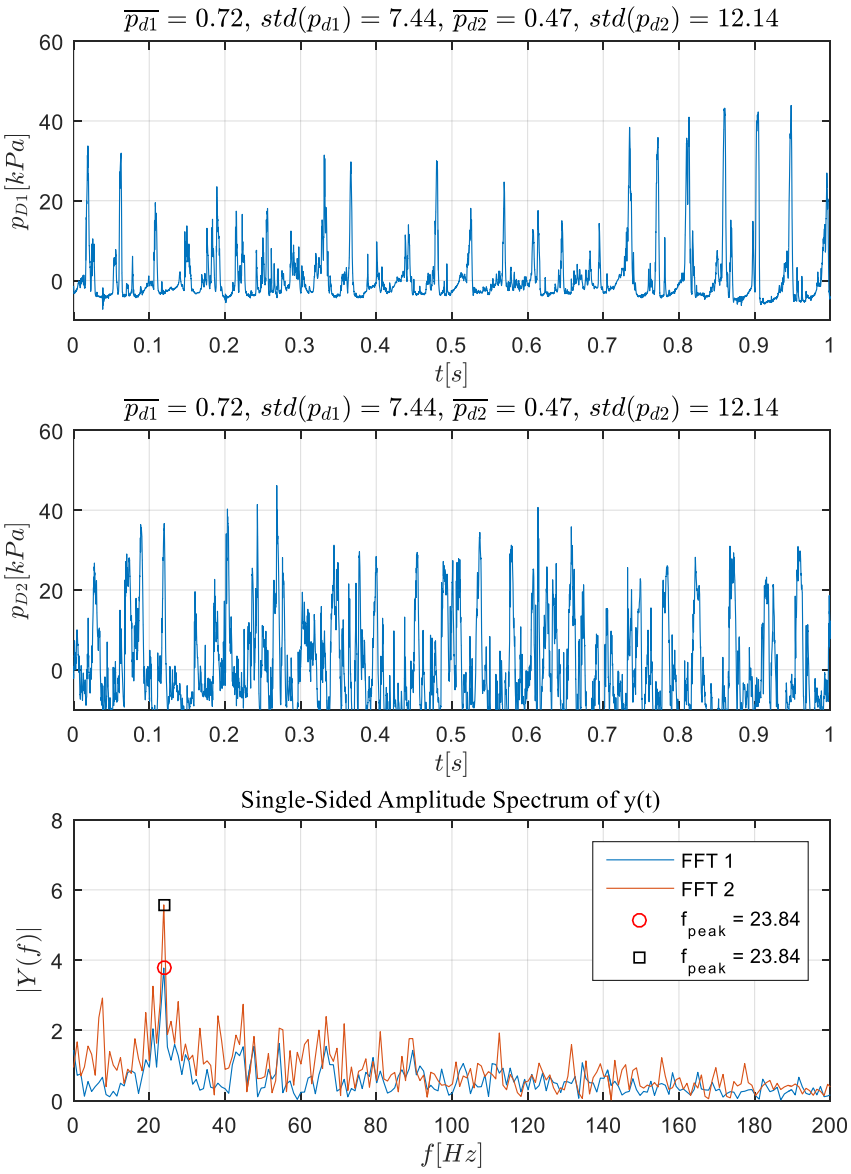

Figure 25: Time-traces of dynamic pressure at p_{d1} and p_{d2}, and their FFTs. *With cavity* injection. (Same case as shown in figures 16a-c and 22). $Q_I/Q_{V,max}$ = 0.07, σ_0 = 2.0 and U_0 = 8 ms^{-1}. The units of averages and standard deviations listed in the titles are (kPa) and (Hz).

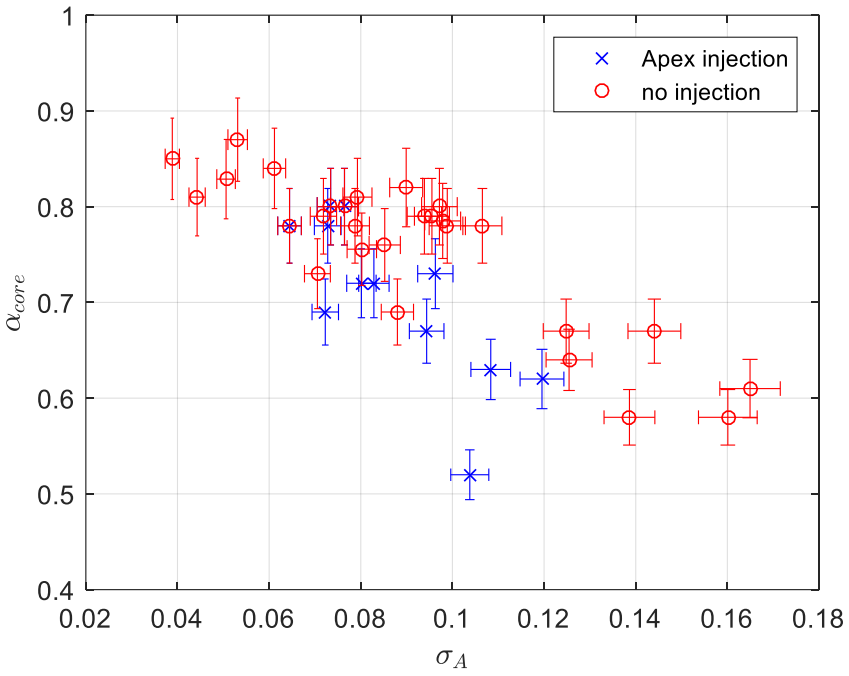

Figure 26: The void fraction upstream of the shock (*i.e.* in the "core" of the cavity) as a function of σ_A for gas injection and the baseline case; $U_0 = 8$ ms^{-1}.

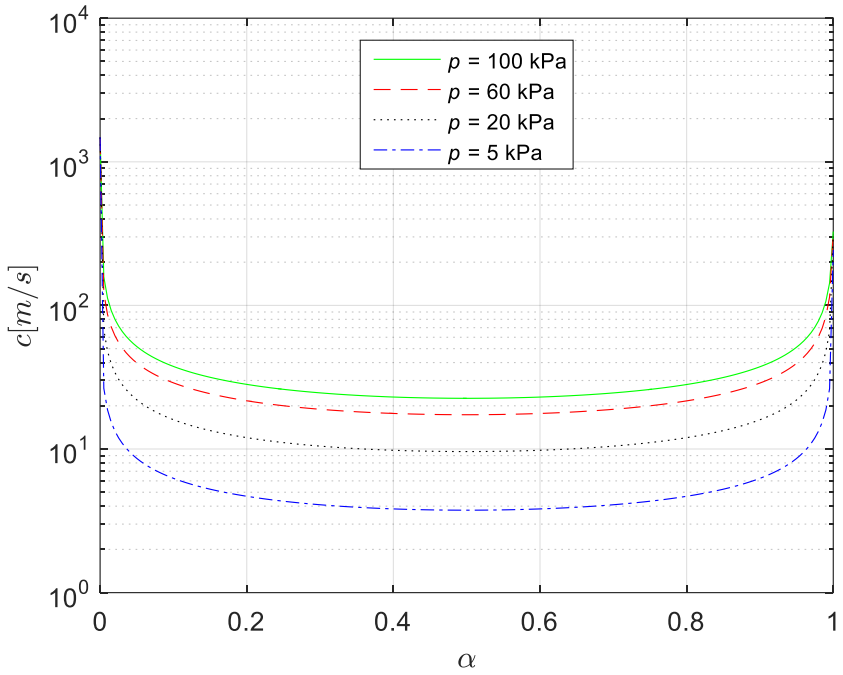

Figure 27: The speed of sound of the bubbly mixture for varying void fraction and pressure assuming the homogeneous frozen model and neglecting bubble dynamics.

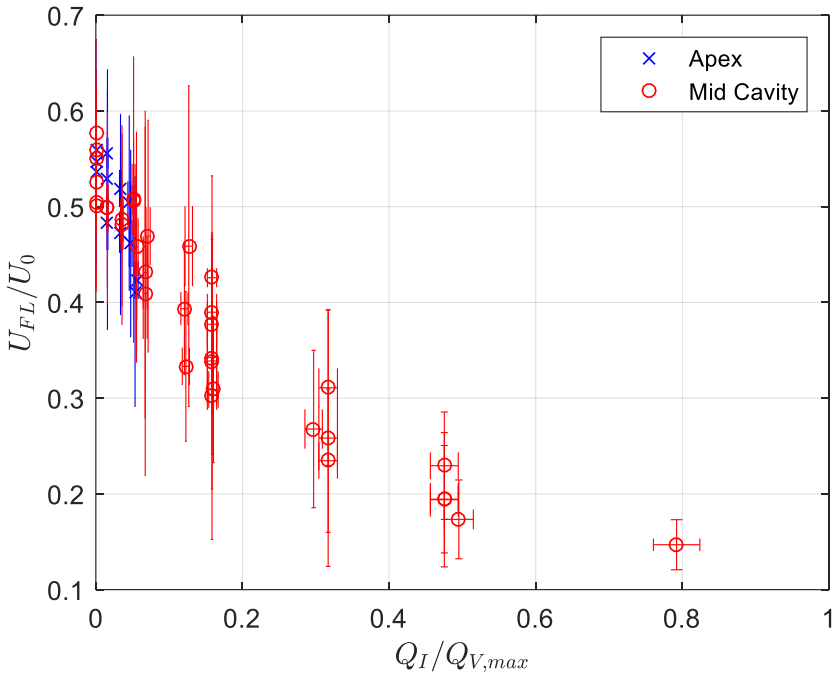

Figure 28: The propagation speed in the laboratory frame of the void fraction discontinuity (which at high gas injection rates may no longer be a bubbly shock), U_{FL} / U_0, as a function of $Q_I/Q_{V,max}$ for apex and cavity injection; σ_0 = 2.0 and U_0 = 8 ms^{-1}.

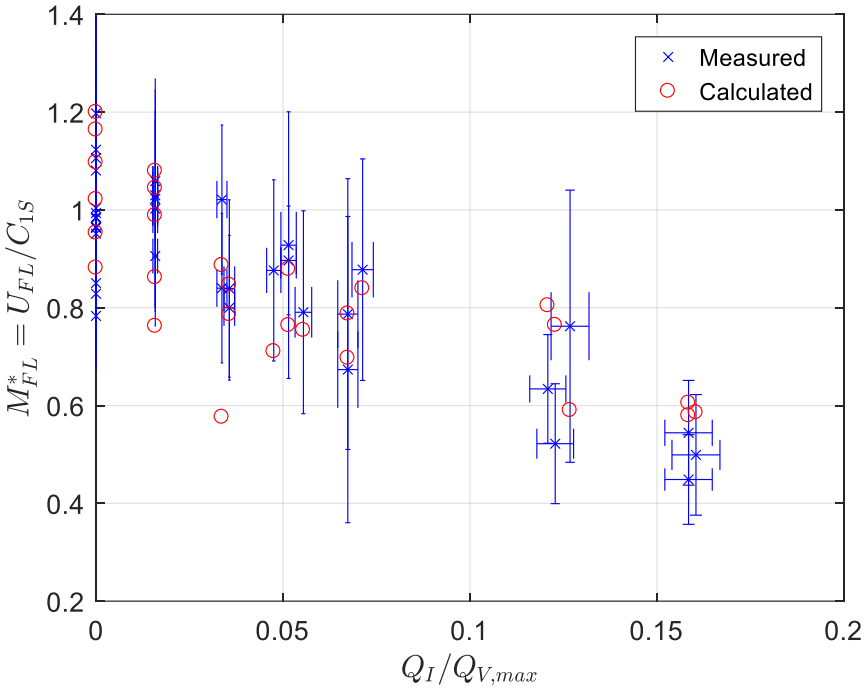

Figure 29: Variation of void fraction discontinuity propagation Mach number in laboratory frame for varying gas injection rates. Also shown are the expected shock speeds based on equation 5.2 (when $p_B > 1.05p_A$), with pressure downstream of shock assumed to be p_B corrected by fraction of time it was covered by cavity (taken to be ~2/3 of the time).

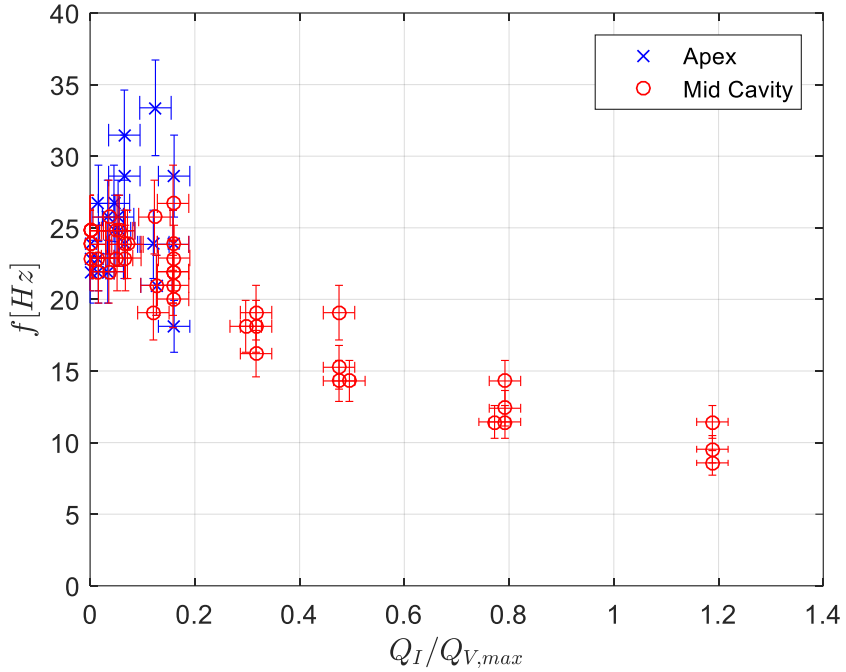

(a)

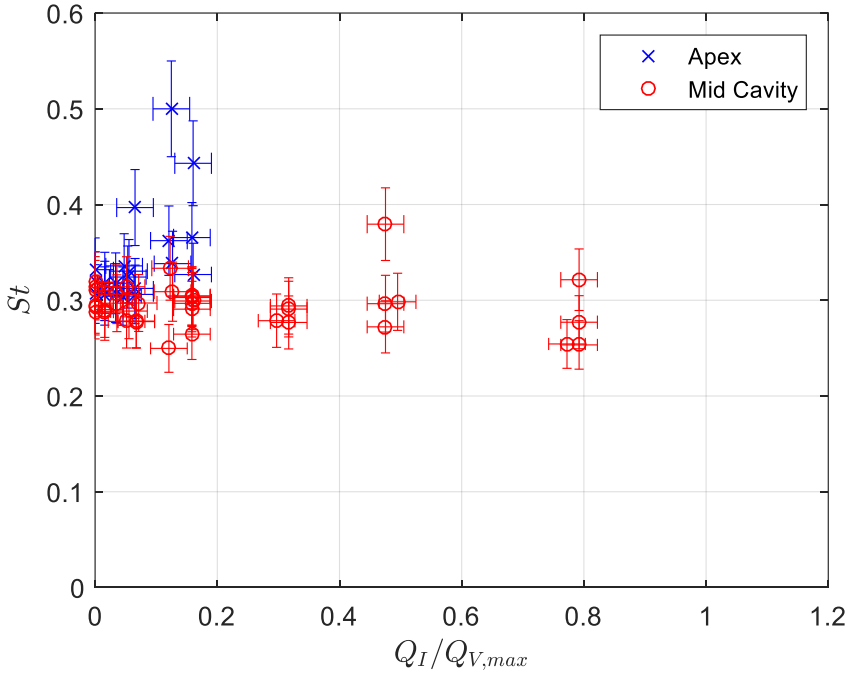

(b)

Figure 30: (a) The shedding frequency and (b) Strouhal number ($L_{10\%} \sim 7.6\ T_{10\%}$) as a function of gas injection rate. Note that in case of the apex injection the cavity became only weakly periodic, and the definition of dominant frequency is not necessarily meaningful.

	Label	s/L_w
Gas injector 1	G_1	0.004
Gas injector 2	G_2	0.134
Static pressure tap A	p_A	0.013
Static pressure tap B	p_B	0.147
Dynamic pressure transducer 1	p_{d1}	0.178
Dynamic pressure transducer 2	p_{d2}	0.464

Table 1: The locations of the gas injectors and instrumentation location on the wedge surface, in wedge coordinates.